El 68 UDC 621.313.33-947:621.3.043.3

ACTA POLYTECHNICA SCANDINAVICA

ELECTRICAL ENGINEERING SERIES No. 68

The High-Speed Induction Motor: Calculating the Effects of Solid-Rotor Material on Machine Characteristics

JUHA PYRHÖNEN

Lappeenranta University of Technology
Department of Energy Technology
P.O.Box 20
SF-53851 Lappeenranta, Finland

HELSINKI 1991

Pyrhönen, J., **The high-speed induction motor: calculating the effects of solid-rotor material on machine characteristics.** Acta Polytechnica Scandinavica, Electrical Engineering Series No. 68, Helsinki 1991, 84 pp. Published by the Finnish Academy of Technology. ISBN 951-666-332-X. ISSN 0001-6845.

Keywords: High speed induction motors, rotor materials.

ABSTRACT

A method for the analysis of high-speed solid-rotor induction motors is presented. The analysis is based on a new combination of the three dimensional linear method and the transfer matrix method. Both saturation and finite length effects are taken into account. The active region of the solid rotor is divided into saturated and unsaturated parts. The time dependence is assumed to be sinusoidal and phasor quantities are used in the solution.

The method is applied to the calculation of smooth solid rotors manufactured of different materials. Six rotor materials are tested: three construction steels, pure iron, a cobalt-iron alloy and an aluminium alloy. The results obtained by the method agree fairly well with the measured quantities.

PREFACE

This work was carried out at the Laboratory of Electric Power Technology, Lappeenranta University of Technology. The work is part of a research project concerning high speed technology that has been studied at the Department of Energy Technology at the Lappeenranta University of Technology.

I wish to express my gratitude to Professor Lauri Aura for his encouregement and Professor Tapani Jokinen for this interesting research topic. I also wish to thank the Finnish Development Pool for Electric Power Technology and the Lappeenranta University of Technology for financing this work. I also thank all persons who have given me aid during the work especially the technical staff of the Laboratory for constructing the test machine.

I am obliged to my friend Mrs. Barbara Miraftabi for language revision as well as to Miss Ulla Ranta for editing this text. Financial support by the Finnish Cultural Foundation is gratefully acknowledged.

Special acknowledgement is given to my wife Sisko Helena for her full support and understanding throughout this work.

Lappeenranta, June 1990

Juha Pyrhönen

CONTENTS

List of symbols

Boldface symbols are used for vectors and symbols of complex variables are overlined.

a	abbreviation	m^{-1}
a_{1k}	factor for calculating the harmonic slot amplitudes	
$\mathbf{A}$	magnetic vector potential	T/m
A	area	m^2
$\mathbf{B}$	magnetic flux density	T
d	depth of penetration	m
D	rotor diameter	m
$\mathbf{D}$	electric flux density	As/m^2
$\mathbf{E}$	electric field strength	V/m
E	electromotive force	V
G	complex constant	Vs/m
$\mathbf{H}$	magnetic field strength	A/m
$\hat{I}$	peak value of stator current	A
$\mathbf{i}, \mathbf{j}, \mathbf{k}$	unit vectors in cartesian co-ordinates	
j	imaginary unit	
$\mathbf{J}$	current density	A/m^2
k_{Cs}	Carter's factor	
K_0	coefficient to calculate linear current density	m^{-1}
K_z	linear current density	A/m
L	stator stack length, rotor length	m
m	number of phases	m
m	ordinal, even	
n	ordinal, odd or the number of the layer	
N	number of turns in series per phase of stator winding	
p	number of pole pairs	
P	power	W/m^2
Q_s	number of stator slots	
r	rotor radius	m
R	resistance	Ω
s	per unit slip	
s	width of the slot opening	m
$\mathbf{S}$	Poynting vector power density	VA/m^2
S'	apparent power	VA

t	time	s
T	torque	Nm
U	voltage	V
V	magnetic voltage	A
X	reactance	Ω
x, y, z	rotor co-ordinates	
x_1, y, z	stator co-ordinates	
Z	impedance	Ω
β	complex coefficient	
β_1	factor for calculating the slot harmonic amplitudes	
γ	complex function, a measure of field variation in the axial direction	
δ	air gap	m
δ_e	equivalent air gap	m
ε	temperature coefficient of resistivity	K^{-1}
Θ	complex coefficient	
θ	magnetomotive force	A
κ_n	even complex function	
κ_m	odd complex function	
λ	complex function of slip associated with the skin depth	
μ	permeability	$\frac{Vs}{Am}$
ν	ordinal of the harmonics	
ξ	winding factor	
ρ	resistivity of rotor material	Ωm
ρ	density	kg/m^3
σ	conductivity	S/m
τ_p	pole pitch of the fundamental	m
τ_s	slot pitch of the stator	m
τ_ν	pole pitch of the ν:th harmonic	m
Φ	magnetic flux	Wb
ω_s	stator angular frequency	s^{-1}
$\omega_{\nu r}$	angular velocity of the νth harmonic in the rotor	s^{-1}
$\omega_{\nu s}$	angular velocity of the νth harmonic in the stator	s^{-1}
Ω	mechanical angular velocity	s^{-1}

1 INTRODUCTION

The Department of Energy Technology at Lappeenranta University of Technology has studied the use of high rotational speeds in energy conversion technology since 1981. In small energy conversion units, the optimum rotational speed is generally very high, in the range of 20 000 rpm to 120 000 rpm. The optimum speed means a speed at which the minimum weight-power ratio and maximum efficiency are reached. Conventional solutions regularly involve a gearbox between the turbomachine (turbine, compressor or pump) and the electric machine. In high speed energy conversion units the turbomachine and the electric machine have a common shaft that rotates at a multiple frequency compared with the synchronous frequency of the common electric network. (Larjola 1988).

High speed electric motors have the advantage of low weight and small size. This makes them attractive for several applications. Despite the advantages of high speed machines, their application at ratings between 5...200 kW is still unusual. There are several serious difficulties for the designer of the machine to overcome:

- At very high speeds centrifugal forces in the rotor become excessive.
- Contactless bearings are usually demanded.
- Cooling a small but powerful machine may be very difficult.

Typical examples of high speed electric machines constructed in Lappeenranta are:

the asynchronous generator	100 kW	30 000 rpm
the turbocompressor motor	50 kW	60 000 rpm
the ultra high speed motor	4 kW	150 000 rpm

A common feature of these machines is the rotor construction. All successful experiments have employed asynchronous rotors of solid construction. These types of rotors are strong enough to tolerate excessive centrifugal forces and rigid enough to keep the first critical frequency above the operating range of the rotor.

Conventional calculation methods have usually been designed for the analysis of cage or wound-rotor induction machines with laminated rotor cores. Evaluation of the machine characteristics is based on a rough idea of the field distribution in the core. These methods do not apply to the analysis of the rotor fields of solid rotor induction motors. The behaviour of solid rotors has been examined widely in the literature during recent decades but so far, high speed solid rotor machines, as they are defined here, have rarely been under consideration.

This research work presents a calculation method to solve Maxwell's equations in steady state operation of the smooth finite length solid rotor. The method is a new combination of the three dimensional linear method and the transfer-matrix method. Both saturation and finite length effects are taken in account. The active region of the solid unslotted rotor without endrings is divided into saturated and unsaturated parts to facilitate the three dimensional solution of the fields. Comparisons between different available rotor materials are made in order to find out the effect of rotor material parameters on the behaviour of the high speed machine.

In the beginning of the work some major limitations of the rotor are considered. Equations to calculate the maximum diameter and length of the rotor are given. In chapters 3, 4 and 5 the theory is gradually developed from a magnetically linear rotor of finite length via a magnetically saturable rotor of infinite length to a rotor which is both saturable and of finite length. Rotor slits and short circuit rings have not been examined at all, because the aim of the study has been to create a calculation method for comparison of different rotor materials. If needed the method can be expanded to include rotor slits, too. A comparison of theoretical and test results of a 12 kW 400 Hz induction machine is given in chapter 8.

2 MAJOR MECHANICAL LIMITATIONS

High speed motors are small and light when compared with conventional 50 Hz motors of the same power. Mechanical stresses occur in the rotor that create major limitations for the rotor design. A normal laminated rotor cannot be used in high speed machines because of its weakness and insufficient rigidness; one must be satisfied with a solid rotor which in electromagnetic terms is much worse than a laminated one but whose mechanical properties are superior.

2.1 Factors limiting the diameter of the rotor

Even though the rotor of a high speed machine is manufactured from a solid piece of metal, the designer cannot ignore the effects of centrifugal force. The maximum stress σ in a cylindrical solid rotor is calculated (Ylinen 1970)

$$\sigma = C \rho r^2 \Omega^2 \tag{1}$$

where

$C = \frac{3+\nu}{8}$ for a smooth homogenous cylinder,

$C = \frac{3+\nu}{4}$ for a cylinder with a small bore,

$C \approx 1$ for a thin cylinder,

ρ is the density of the material,
r is the radius of the rotor,
Ω is the angular velocity of the rotor,
ν is Poisson's coefficient.

Poisson's coefficients for some pure metals are given in Table 1.

Table 1. Poisson's coefficients for some pure metals.

Metal		ν	Metal		ν
Aluminium	Al	0.34	Nickel	Ni	0.30
Copper	Cu	0.34	Titanium	Ti	0.34
Iron	Fe	0.29	Cobalt	Co	0.31

2.2 The length of the rotor

The length of the rotor is limited by specific frequencies. Often the dimensions of the rotor are chosen so that it can operate below the first critical speed which corresponds to the first specific frequency. If the construction and bearings of the machine pass the first critical speed, the rotor can be operated between the first and the second specific frequencies. This demands a very high load capacity of the bearings. The maximum length L of the rotor is given by the following equation (Wiart 1982):

$$L^2 = n^2 \frac{\pi^2}{k\,\Omega} \sqrt{\frac{E\,I}{\rho\,A}} \qquad (2)$$

where A is the area of the cross-section of the cylinder (m^2),
E is the modulus of elasticity (N/m^2),
I is the modulus of inertia (m^4),
n is the number of the critical speed,
$k = \Omega_c/\Omega_n$ is the ratio between the n:th critical angular velocity and the nominal angular velocity; safety factor.

If safety factor k_σ is used for the maximum allowable stress in the rotor, the ratio L/r can be found using Eqns. 1 and 2:

$$\frac{L}{r} = n\,\pi \sqrt{\frac{k_\sigma}{k}}\ \sqrt[4]{\frac{CE}{4\,\sigma}}\,. \tag{3}$$

This ratio determines the relationship between the maximum length and the maximum radius of the rotor. L/r is not a function of the angular velocity, and for a cylindrical rotor made of steel this ratio is about 7, and in practice about 5, when the rotor is operating below the first critical speed.

3 THE SOLUTION OF THE ROTOR FIELDS UNDER CONSTANT PERMEABILITY

In the following analysis an analytical solution of Maxwell's equations is found for a smooth rotor of finite length. The rotor is not equipped with short circuit rings. As a boundary condition it has been assumed that no flux penetrates into the rotor's endfaces. This is an approximation that has been tested by Yee (1971). The field solutions are approximate, because the solution in closed form becomes impossible without some simplifications.

These simplifications are:

1. The rotor material is assumed to be linear so its relative permeability μ_r and conductivity σ are constants. The material is homogenous and isotropic. There is no hysteresis.
2. The surface of the rotor is smooth.
3. The curvature of the rotor is ignored and the stator and rotor are expanded into flat, infinitely thick bodies. Equations are written in cartesian co-ordinates.
4. The stator has an infinite permeability in the direction of the laminations.
5. The stator windings and currents create an infinitesimally thin sinusoidal current sheet on the surface of the stator bore. This current sheet does not vary axially.

6. The flux density normal to the endfaces is zero.
7. The radial flux density in the air gap does not vary radially. The mistake made here is quite small when the air gap is small compared to the diameter of the rotor.

The solution is found in a form of Fourier-series. The following aspects must be noted: Several solutions are found; a particular solution is found when sufficient boundary conditions, usually at the rotor surfaces, are determined. The boundary conditions used give the advantage of avoiding the need to examine how the stator windings continue outside the stator stack length. The solution is not valid outside the rotor. This method was first used by Bondi and Mukherji (1957) and later developed by Yee (1971).

3.1 The co-ordinate system

In the following co-ordinates fixed with both the rotor and the stator (x, y, z) and (x_1, y, z) are used respectively; x is fixed with the rotor and x_1 with the stator. The origin of the rotor co-ordinates is at the surface of the rotor and axially (z) at its midpoint, Fig. 1.

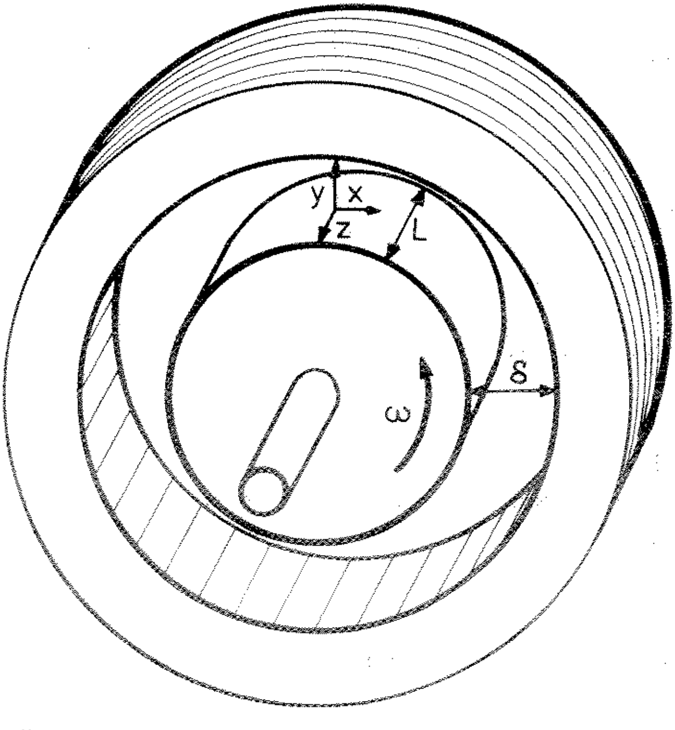

Figure 1. Co-ordinates at the surface of the rotor.

When the rotor is rotating at a slip s in the direction of the negative x-axis, the relationship between x and x_1 may be written as follows (Richter 1954):

$$x_1 = x - (1-s)\omega_s t \frac{r}{p} , \tag{4}$$

where p is number of pole pairs
r is rotor radius
s is per unit slip
t is time
ω_s is stator angular frequency

By using the abbreviation a and the pole pitch τ_p

$$a = \frac{\pi}{\tau_p} \quad , \quad \tau_p = \frac{2\pi r}{2p} , \tag{5}$$

Eqn. 4 can be rewritten

$$ax_1 + \omega_s t = ax + s\omega_s t . \tag{6}$$

The stator current creates a linear current density K_z which can be written in amperes per metre.

$$K_z = \mathrm{Re}\left\{ K_0 \hat{I} e^{j(ax_1 + \omega_s t)} \right\} , \tag{7}$$

where $\hat{I}$ is the peak value of the stator current and

$$K_0 = \frac{m}{p \tau_p} (\xi N) = \frac{m}{\pi p} (\xi N) a . \tag{8}$$

Here m is number of phases
N is number of turns in series per phase of stator winding
ξ is winding factor.

3.2 General solution for the rotor fields using linear magnetization

General equations of the field that James Clerk Maxwell derived in 1860's must be used as a starting point. Maxwell's differential equations relate magnetic field strength **H** with current density **J** and electric field density **D** and also electric field strength **E** with magnetic flux density **B**. The equations also determine the divergence of **B** and **E**.

$$\nabla\times\mathbf{H} = \mathbf{J} + \left(\frac{\partial}{\partial t}\mathbf{D}\right) , \tag{9a}$$

$$\nabla\times\mathbf{E} = -\frac{\partial \mathbf{B}}{\partial t} , \tag{9b}$$

$$\nabla\cdot\mathbf{B} = 0 , \tag{9c}$$

$$\nabla\cdot\mathbf{E} = 0 , \tag{9d}$$

The latter part of Eqn. 9a representing Maxwell's displacement current is omitted, because it is negligible compared with the conducting current at frequencies which do occur in the machine. Solutions are obtained here using the magnetic vector potential **A**, which is defined by

$$\nabla\times\mathbf{A} = \mathbf{B} , \tag{10a}$$

$$\nabla\cdot\mathbf{A} = 0 . \tag{10b}$$

The material equations can be expressed using conductivity σ, relative permeability μ_i and the permeability of free space μ_0

$$\sigma\mathbf{E} = \mathbf{J} , \tag{11a}$$

$$\mu_i\mu_0\,\mathbf{H} = \mu\mathbf{H} = \mathbf{B} . \tag{11b}$$

Keeping μ and σ as constants the differential equation for vector potential **A** is obtained by using Eqns. 9 and 10.

$$\nabla(\nabla\cdot\mathbf{A}) - \nabla^2\mathbf{A} = -\mu\sigma\frac{\partial}{\partial t}\mathbf{A} . \tag{12}$$

Because the divergence of the vector potential is equal to zero and the Laplace operator is $\nabla^2 = \frac{\partial^2}{\partial x^2} + \frac{\partial^2}{\partial y^2} + \frac{\partial^2}{\partial z^2}$, the second order differential equation is found as

$$\frac{\partial^2 A_i}{\partial x^2} + \frac{\partial^2 A_i}{\partial y^2} + \frac{\partial^2 A_i}{\partial z^2} = \mu\sigma \frac{\partial A_i}{\partial t} \quad , \tag{13}$$

where i is x, y or z.

In steady state a time-harmonic solution for the vector potential in the rotor is found. **A** also varies sinusoidally with x in the rotor, thus expressed as a complex exponential function

$$\mathbf{A}(x, y, z, t) = \overline{\mathbf{A}}(y, z)\, e^{j\,(ax+s\omega_s t)} \tag{14}$$

2

Differentiating Eqn. 14 gives the opportunity to rewrite Eqn. 13 in the complex plane

$$\frac{\partial^2 \overline{A}_i}{\partial y^2} + \frac{\partial^2 \overline{A}_i}{\partial z^2} = a^2\, \overline{A}_i + j\mu\sigma\omega_s s\overline{A}_i \,. \tag{15}$$

Using the annotation

$$\lambda^2 = j\omega_s s\mu\sigma = \frac{j}{\left[\frac{1}{\sqrt{\omega_s s\mu\sigma}}\right]^2} = j\frac{1}{d^2} \tag{16}$$

where d is the depth of penetration, Eqn. 15 can be rewritten

$$\frac{\partial^2 \overline{A}_i}{\partial y^2} + \frac{\partial^2 \overline{A}_i}{\partial z^2} = (a^2 + \lambda^2)\, \overline{A}_i \,. \tag{17}$$

The divergence equation for $\overline{A}$ in cartesian co-ordinates is

$$\nabla \cdot \overline{A} = \frac{\partial \overline{A}_x}{\partial x} + \frac{\partial \overline{A}_y}{\partial y} + \frac{\partial \overline{A}_z}{\partial z} = 0. \tag{18}$$

In deriving the solution for the rotor fields the necessary boundary conditions into the solution are chosen in a convenient manner as:

(1) The current has no axial component at the ends of the rotor, i.e.

$$\overline{E}_z = \overline{A}_z = 0 \text{, when } z = \pm \frac{L}{2} . \tag{19}$$

(2) The magnetic flux density has no axial component at the ends of the rotor, i.e.

$$\overline{B}_z = 0 \text{, when } z = \pm \frac{L}{2} . \tag{20}$$

(3) Because of the symmetry of the machine about the xy-plane, the following conditions of symmetry apply:

roska $E = - \frac{\partial A}{dt}$

(a) $\overline{A}_x (z) = -\overline{A}_x (-z)$

(b) $\overline{A}_y (z) = -\overline{A}_y (-z)$ (21)

(c) $\overline{A}_z (z) = \overline{A}_z (-z)$.

(4) Since the flux attenuates when it penetrates into the conducting material, the following condition applies:

$$\lim_{y \to -\infty} \overline{A}, \overline{B} = 0 . \tag{22}$$

The superposition principle can be employed to simplify the mathematics in obtaining a solution for the rotor fields. Separate solutions for the following three cases are found:

(1) $\overline{A}_z \neq 0 , \overline{B}_z = 0$

(2) $\overline{A}_z = 0 , \overline{B}_z \neq 0$

(3) $\overline{A}_z = 0 , \overline{B}_z = 0$.

Any general case of flux distribution in a linear electromagnetic circuit can be presented with these three types of fields. The complete general solution is then found by superposition of the three solutions. The next presentation is usually simplified by leaving factor $e^{j(ax + s\omega_s t)}$ out. It must, however, be remembered at all times.

3.2.1 The solution of rotor fields, when $\overline{A}_z \neq 0$ and $\overline{B}_z = 0$

Because $\overline{A}_z(z) = \overline{A}_z(-z)$ according to Eqn. 21c., $\overline{A}_z$ may be written as a Fourier-series in z using cosine terms only. To apply the condition of Eqn. 19 $\overline{E}_z = \overline{A}_z = 0$, when $z = \pm\frac{L}{2}$, it is convenient to take 2L as the fundamental wave length and to use odd terms only. Thus

$$\overline{A}_z = \sum_{n=1,3...}\left\{ f(y,n)\cos(n\pi z/L) \right\} . \tag{23}$$

Since the solution for the component $\overline{A}_z$ of Eqn. 17 is first searched, we write

$$\frac{\partial^2\overline{A}_z}{\partial y^2} + \frac{\partial^2\overline{A}_z}{\partial z^2} = (a^2+\lambda^2)\,\overline{A}_z \cdot \tag{24}$$

The method of separating variables is used and the solution for $\overline{A}_z$ is written using aid functions $\overline{H}$ and $\overline{Q}$

$$\overline{A}_z\,(y,z) = \overline{H}(y)\,\overline{Q}(z) . \tag{25}$$

After substituting this in Eqn. 24 separating the variables gives

$$\frac{1}{\overline{H}}\frac{\partial^2\overline{H}}{\partial y^2} = -\frac{1}{\overline{Q}}\left(\frac{\partial^2\overline{Q}}{\partial z^2} - (a^2+\lambda^2)\overline{Q}\right) = -k^2 . \tag{26}$$

The expression on the left involves functions dependent only on y while the expression on the right involves functions only on z. Hence both expressions must be equal to a constant. This immediately yields two ordinary linear differential equations for $\overline{H}$ and $\overline{Q}$, namely

$$\frac{\partial^2\overline{H}}{\partial y^2} + k^2\,\overline{H} = 0 ,$$

$$\frac{\partial^2\overline{Q}}{\partial z^2} - (a^2+\lambda^2+k^2)\,\overline{Q} = 0 . \tag{27}$$

The annotation p^2 is employed

$$p^2 = -(a^2 + \lambda^2 + k^2)\,. \tag{28}$$

General solutions for these Eqns. are of the form: $\overline{H}(y) = R\cos(ky) + S\sin(ky)$ and, $\overline{Q}(z) = T\cos(pz) + U\sin(pz)$, where R, S, T and U are constants. Because a Fourier-series in z containing cosine terms only is searched, it is marked that $U = 0$ and $T \neq 0$ in order to get a nonzero solution. Thus $\overline{Q}(z)$ is

$$\overline{Q}\,(z) = T\cos\,(pz)\,. \tag{29}$$

According to condition 19 it is found that

$$p = n\,\frac{\pi}{L}\,,\ \text{where } n = 1, 3, 5\ldots\ . \tag{30}$$

The solution for k is now found by using Eqn. 28

$$k = j\sqrt{\left(n\,\frac{\pi}{L}\right)^2 + j\omega_s s\mu\sigma + a^2}\ . \tag{31}$$

This yields

$$\overline{H}(y) = R\cos j\sqrt{\left(n\,\frac{\pi}{L}\right)^2 + j\omega_s s\mu\sigma + a^2}\;y + S\sin j\sqrt{\left(n\,\frac{\pi}{L}\right)^2 + j\omega_s s\mu\sigma + a^2}\;y\,. \tag{32}$$

Since $\cos(jy) = \cosh(y)$ and $\sin(jy) = j\sinh(y)$, using the condition of Eqn. 22 gives $S = -jR$. Now, if a_n contains all constants, the solution for $\overline{A}_z$ is found to be

$$\overline{A}_z = \sum_{n=1,3\ldots} a_n e^{\sqrt{a^2 + \left(n\,\frac{\pi}{L}\right)^2 + \lambda^2}\;y} \cos\left(\frac{n\pi z}{L}\right) e^{\,j(ax+s\omega_s t)}\,. \tag{33}$$

The following annotation will be used

$$\kappa_n = \sqrt{a^2 + \left(n\,\frac{\pi}{L}\right)^2 + \lambda^2}\ . \tag{34}$$

Solutions for $\overline{A}_x$ and $\overline{A}_y$ must be found next. The equations needed are Eqn. 17, Eqn. 18 and Eqn. 22. Since $\overline{B}_z = 0$, the curl Eqn. 10a gives the following condition

$$\frac{\partial \overline{A}_y}{\partial x} - \frac{\partial \overline{A}_x}{\partial y} = 0 . \tag{35}$$

In addition, the condition of Eqn. 21 applies. Proceeding analogously gives solutions for $\overline{A}_x$ and $\overline{A}_y$. The solutions together are

$$\overline{A}_x = \sum_{n=1,3...} S' e^{\kappa_n y} \sin\left(\frac{n\pi z}{L}\right) e^{j(ax+s\omega_s t)} ,$$

$$\overline{A}_y = \sum_{n=1,3...} R' e^{\kappa_n y} \sin\left(\frac{n\pi z}{L}\right) e^{j(ax+s\omega_s t)} , \tag{36}$$

$$\overline{A}_z = \sum_{n=1,3...} a_n e^{\kappa_n y} \cos\left(\frac{n\pi z}{L}\right) e^{j(ax+s\omega_s t)} .$$

By substituting solution 36 in Eqns. 18 and 35, solutions for R' and S' can be obtained

$$R' = \frac{S'\kappa_n}{ja} = \frac{n a_n}{n^2 + (L\lambda/\pi)^2} \frac{L}{\pi} \kappa_n ,$$

$$S' = \frac{n a_n}{n^2 + (L\lambda/\pi)^2} \frac{ja L}{\pi} . \tag{37}$$

So the solution for the first type of field has been obtained.

3.2.2 The solution of rotor fields when $\overline{A}_z = 0$ and $\overline{B}_z \neq 0$

According to Eqn. 10a it can be written for the axial component of the magnetic flux density

$$\overline{B}_z(z) = \frac{\partial}{\partial x} \overline{A}_y (z) - \frac{\partial}{\partial y} \overline{A}_x (z) \tag{38}$$

This together with Eqn. 21 implies that $\overline{B}_z(z) = -\overline{B}_z(-z)$, and $\overline{B}_z$ may therefore be expressed as a Fourier series in z using sin-terms only. Since $\overline{B}_z = 0$, when $z = \pm L/2$ according to Eqn. 20, the Fourier-series contains even terms only.

$$\overline{B}_z = \sum_{m=2,4,6\ldots} g(y,m) \sin(m\pi z/L) . \tag{39}$$

Eqns. 9 and 10 give the following relations

$$\overline{\mathbf{E}} = -\frac{\partial}{\partial t}\overline{\mathbf{A}} . \tag{40}$$

$$\nabla\times\overline{\mathbf{B}} = -\mu\sigma\frac{\partial\overline{\mathbf{A}}}{\partial t} . \tag{41}$$

Since $\overline{A}_z \equiv 0$, also, its time derivative is zero

$$\frac{\partial\overline{A}_z}{\partial t} = 0 . \tag{42}$$

Eqn. 41 now gives

$$\frac{\partial\overline{B}_y}{\partial x} - \frac{\partial\overline{B}_x}{\partial y} = 0 . \tag{43}$$

In addition equation which is of the same form as Eqn. 17 is valid for the magnetic field density $\overline{\mathbf{B}}$

$$\frac{\partial^2\overline{B}_i}{\partial y^2} + \frac{\partial^2\overline{B}_i}{\partial z^2} = (a^2 + \lambda^2)\,\overline{B}_i , \tag{44}$$

$\overline{B}_x$, $\overline{B}_y$, $\overline{B}_z$, individually satisfy Eqn. 44. Together with Eqn. 43 and the divergence equation for flux density $\overline{\mathbf{B}}$. The solution proceeds analogously with the previous ones. Factor $m\pi/L$ is added to simplify further mathematics.

$$\overline{B}_x = R' \frac{m\pi}{L} e^{\kappa_m y} \cos(m\pi z/L) , \tag{45}$$

$$\overline{B}_y = b_m \frac{m\pi}{L} e^{\kappa_m y} \cos(m\pi z/L) , \tag{46}$$

$$\overline{B}_z = S' \frac{m\pi}{L} e^{\kappa_m y} \sin(m\pi z/L) , \tag{47}$$

where κ_m has an analog form with Eqn. 34 and b_m is a constant. Substitution in Eqn. 43 gives

$$R' = \frac{ja \ b_m}{\kappa_m} . \tag{48}$$

Divergence equation 9c gives the solution for S'

$$S' = \frac{a^2 b_m L - \ b_m \kappa_m^2 L}{\kappa_m \, m\pi} . \tag{49}$$

Now the following equations are achieved for the flux densities, when $\overline{A}_z = 0$ and $\overline{B}_z \neq 0$

$$\overline{B}_x = \sum_{m=2,4,6...} \frac{ja \ b_m}{\kappa_m} \frac{m\pi}{L} e^{\kappa_m y} \cos(m\pi z/L) \, e^{j(ax+s\omega_s t)} , \tag{50}$$

$$\overline{B}_y = \sum_{m=2,4,6...} b_m \frac{m\pi}{L} e^{\kappa_m y} \cos(m\pi z/L) \, e^{j(ax+s\omega_s t)} , \tag{51}$$

$$\overline{B}_z = \sum_{m=2,4,6...} \frac{a^2 b_m - \ b_m \kappa_m^2}{\kappa_m} e^{\kappa_m y} \cdot \sin(m\pi z/L) \, e^{j(ax+s\omega_s t)} . \tag{52}$$

In this case, when $\overline{A}_z = 0$, according to Eqn. 10a the following solution for $\overline{A}_x$ and $\overline{A}_y$ is found:

$$\begin{aligned} \overline{A}_x &= \sum_{m=2,4,6...} b_m \, e^{\kappa_m y} \cos(m\pi z/L) \, e^{j(ax+s\omega_s t)} , \\ \overline{A}_y &= \sum_{m=2,4,6...} \frac{ja \ b_m}{\kappa_m} e^{\kappa_m y} \cos(m\pi z/L) \, e^{j(ax+s\omega_s t)} . \end{aligned} \tag{53}$$

3.2.3 The solution of the rotor fields when $\overline{A}_z = \overline{B}_z = 0$

Because $\overline{A}_z \equiv 0$, the divergence Eqn. 10b gives

$$\frac{\partial \overline{A}_x}{\partial x} + \frac{\partial \overline{A}_y}{\partial y} = 0 . \tag{54}$$

Because $\overline{B}_z \equiv 0$, the curl Eqn. 10a gives

$$\frac{\partial \overline{A}_y}{\partial x} - \frac{\partial \overline{A}_x}{\partial y} = 0 . \tag{55}$$

Eqns. 17, 54 and 55 give

$$\overline{A}_x = e^{ay} \left(R \cosh(\lambda z) + S \sinh(\lambda z)\right) \tag{56}$$

The condition of Eqn. 21(a) requires that the constant R = 0; therefore the solution for this special case $\overline{A}_z = \overline{B}_z = 0$ is

$$\overline{A}_x = G\, e^{ay} \sinh(\lambda z)/\sinh(\lambda L/2)\, e^{j(ax+s\omega_s t)} , \tag{57}$$

$$\overline{A}_y = jG\, e^{ay} \sinh(\lambda z)/\sinh(\lambda L/2)\, e^{j(ax+s\omega_s t)} ,$$

where G is a complex constant. The other constant sinh(λL/2) is added to simplify further mathematics.

Now the complete general solution can be written. The following two annotations are used for simplicity

$$\sum_{n=1,3,5...} = \sum_{n} \text{ and} \sum_{m=2,4,6...} = \sum_{m} .$$

$$\overline{A}_x = \sum_n \frac{n a_n}{n^2 + (L\lambda/\pi)^2} \frac{ja\, L}{\pi} e^{\kappa_n y} \sin(n\pi z/L) e^{j(ax+s\omega_s t)}$$

$$+ \sum_m b_m\, e^{\kappa_m y} \sin(m\pi z/L)\, e^{j(ax+s\omega_s t)}$$

$$+ G\, e^{ay} \sinh(\lambda z)/(\sinh(\lambda L/2))\;\; e^{j(ax+s\omega_s t)} , \tag{58}$$

$$\overline{A}_y = \sum_n \frac{na_n}{n^2+(L\lambda/\pi)^2} \frac{L\,\kappa_n}{\pi} e^{\kappa_n y} \sin(n\pi z/L)\, e^{j(ax+s\omega_s t)}$$

$$-\sum_m b_m \frac{j\,a}{\kappa_m} e^{\kappa_m y} \sin(m\pi z/L)\, e^{j(ax+s\omega_s t)}$$

$$-j\,G\,e^{ay} \sinh(\lambda z)/(\sinh(\lambda L/2))\;\; e^{j(ax+s\omega_s t)}\;, \tag{59}$$

$$\overline{A}_z = \sum_n a_n\, e^{\kappa_n y} \cos(n\pi z/L)\, e^{j(ax+s\omega_s t)}\,. \tag{60}$$

3.3 Approximate solution

To facililitate the following analysis, some simplifications must be introduced at this point. The simplifications are valid when the ratio between the depth of penetration and the pole pitch is small.

$$\left|\lambda^2\right| >> a^2 \tag{61}$$

$$\left|\lambda^2\right| >> (n\pi/L)^2 \text{ or } (m\pi/L)^2 \tag{62}$$

Inequalities 61 and 62 both hold except at very small slips. The use of these inequalities greatly simplifies further mathematics. The first simplification is found as

$$\kappa_n \approx \kappa_m \approx \lambda \tag{63}$$

By using Eqn. 63, equations 58...60 are greatly simplified since the factors $\exp(\kappa_n y)$ and $\exp(\kappa_m y)$ can be brought outside the summation signs. Equations 58...60 then become

$$\overline{A}_x = \frac{ja\,L}{\pi} e^{\lambda y} \sum_n \frac{na_n}{n^2+(L\lambda/\pi)^2} \sin(n\pi z/L) +$$

$$+ e^{\lambda y} \sum_{m} b_m \sin(m\pi z/L)$$

$$+ G\, e^{ay} \sinh(\lambda z)/\sinh(\lambda L/2) \,, \tag{64}$$

$$\overline{A}_y = \frac{L\lambda}{\pi} e^{\lambda y} \sum_{n} \frac{n a_n}{n^2 + (L\lambda/\pi)^2} \sin(n\pi z/L)$$

$$- \frac{j\, a}{\lambda} e^{\lambda y} \sum_{m} b_m \sin(m\pi z/L)$$

$$- j\, G\, e^{ay} \sinh(\lambda z)/\sinh(\lambda L/2) \;, \tag{65}$$

$$\overline{A}_z = e^{\lambda y} \sum_{n} a_n \cos(n\pi z/L) \;. \tag{66}$$

According to Eqn. 10a the approximate expressions for $\overline{B}$ are

$$\overline{B}_x = \lambda\, e^{\lambda y} \frac{L^2 \lambda^2}{\pi^2} \sum_{n} \frac{a_n}{n^2 + (L\lambda/\pi)^2} \cos(n\pi z/L)$$

$$+ \frac{j\, a\, \pi}{\lambda L} e^{\lambda y} \sum_{m} m\, b_m \cos(m\pi z/L)$$

$$+ jG\lambda e^{ay} \cosh(\lambda z)/\sinh(\lambda L/2) \;, \tag{67}$$

$$\overline{B}_y = -ja \frac{L^2 \lambda^2}{\pi^2} e^{\lambda y} \sum_{n} \frac{a_n}{n^2 + (L\lambda/\pi)^2} \cos(n\pi z/L)$$

$$+ \frac{\pi}{L} e^{\lambda y} \sum_{m} b_m\, m \cos(m\pi z/L)$$

$$+ G\lambda e^{ay} \cosh(\lambda z)/\sinh(\lambda L/2) \;, \tag{68}$$

$$\overline{B}_z = \frac{a^2 - \lambda^2}{\lambda} e^{\lambda y} \sum_{m} b_m \sin(m\pi z/L) \;. \tag{69}$$

3.4 The relation between the rotor and stator fields

Ampère's law for quasi stationary fields is

$$\int_{C'} \mathbf{H}\cdot d\mathbf{l} = \int_{S} \mathbf{J}\cdot d\mathbf{S} = \Sigma I \tag{70}$$

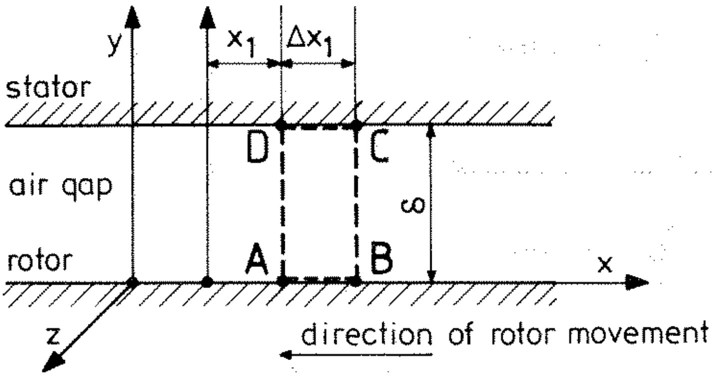

Figure 2. Application of Ampère's circuital law around the integration path C': A B C D A

To determine the constants a_n, b_m and G additional boundary conditions are required. Application of Ampère's circuital law in the air gap around path ABCDA in Fig. 2 yields the following relation for the air gap fields with respect to the stator axes:

$$\overline{K}_z \Delta x_1 = \overline{H}_{\delta x}(y=0)\Delta x_1 + \int_0^{\delta} \overline{H}_{\delta y}(x_1+\Delta x_1)dy + \int_{\delta}^{0} \overline{H}_{\delta y}(x_1)dy$$

$$= \overline{H}_{\delta x}(y=0)\Delta x_1 + \int_0^{\delta} \overline{H}_{\delta y}(x_1+\Delta x_1)dy - \int_0^{\delta} \overline{H}_{\delta y}(x_1)dy\,. \tag{71}$$

Since $\overline{H}_y$ is assumed not to be a function of y in the air gap, it can be written according to the definition of derivative

$$\overline{K}_z \Delta x_1 = \overline{H}_{\delta x}(y=0)\Delta x_1 + \int_0^{\delta} \frac{\partial \overline{H}_{\delta y}}{\partial x_1} \Delta x_1 \; dy$$

$$= \overline{H}_{\delta x}(y=0)\Delta x_1 + \delta \; \frac{\partial \overline{H}_{\delta y}}{\partial x_1} \Delta x_1 \, . \qquad (72)$$

The current sheet is now

$$\overline{K}_z = \left(\overline{H}_{\delta x} + \frac{\delta}{\mu_0} \; \frac{\partial \; \overline{B}_{\delta y}}{\partial \; x_1} \right)_{y=0} . \qquad (73)$$

Since at $y = 0$, $\overline{H}_{\delta x} = \overline{H}_x$ and $\overline{B}_{\delta y} = \overline{B}_y$, Eqn. 73 forms a boundary condition for the rotor fields. Eqn. 73 can also be written in rotor co-ordinates:

$$\overline{K}_z = \left(\overline{H}_x + \frac{\delta}{\mu_0} \; \frac{\partial \; \overline{B}_y}{\partial x} \right)_{y=0} . \qquad (74)$$

The other boundary condition is obviously

$$\overline{A}_y(y{=}0) = \overline{E}_y(y{=}0) = 0 \, . \qquad (75)$$

This is a necessary condition to get the normal component of current at the rotor surface to be zero. Eqn. 74 is more easily evaluated by using partial differentiation with respect to z. When $y = 0$, the following can be written:

$$\frac{\partial \overline{K}_z}{\partial z} = \left(\frac{\partial \overline{H}_x}{\partial z} + \frac{\delta}{\mu_0} \, \frac{\partial}{\partial z} \, \frac{\partial \overline{B}_y}{\partial x} \right)_{y=0} = \left(\frac{\partial \overline{H}_x}{\partial z} + \frac{\delta}{\mu_0} \, \frac{\partial}{\partial x} \, \frac{\partial \overline{B}_y}{\partial z} \right)_{y=0} . \qquad (76)$$

Since $\nabla \times \overline{B} = -\mu\sigma \frac{\partial \overline{A}}{\partial t}$ according to Eqns. 9 and 10 the following can be written at the rotor surface ($y = 0$) when $\overline{A}_y$ is identically zero:

$$\frac{\partial}{\partial x} \overline{B}_z - \frac{\partial}{\partial z} \overline{B}_x = 0 \qquad (77)$$

During the following operations the constants of Eqn. 86 are denoted by M and N.

$$\int_{-\frac{L}{2}}^{\frac{L}{2}} \sum_{m} b_m \, M \sin(\frac{\alpha\pi}{L} z) \sin(\frac{m\pi}{L}) \, dz = \int_{-\frac{L}{2}}^{\frac{L}{2}} N \sin(\frac{\alpha\pi}{L} z) \sinh(\lambda z) dz \, . \tag{88}$$

The left side of Eqn. 88 can be written

$$\frac{1}{2}\sum_{m} \int_{-\frac{L}{2}}^{\frac{L}{2}} b_m M \cos(\frac{m\pi}{L} - \frac{\alpha\pi}{L}) z \, dz - \frac{1}{2} \sum_{m} \int_{-\frac{L}{2}}^{\frac{L}{2}} b_m M \cos(\frac{m\pi}{L} + \frac{\alpha\pi}{L}) z \, dz \, . \tag{89}$$

The latter part of this is equal to zero. The former term is always equal to zero, when a $\neq$ m, and is equal to 1/4 b_m ML , when $\alpha = m$. Now the following can be written for b_m:

$$b_m = \frac{4\,N}{ML} \int_{-\frac{L}{2}}^{+\frac{L}{2}} \frac{1}{2} (e^{\lambda z} - e^{-\lambda z}) \sin(\frac{\alpha\pi}{L} z) dz \, . \tag{90}$$

After having evaluated the integral, b_m is written after substitution of M and N

$$b_m = \frac{(-1)^{\frac{m}{2} - 1}}{m^2 + (\frac{\lambda L}{\pi})^2} \; \frac{4m}{m^2 - \frac{(\frac{La}{\pi})^2}{\delta \lambda \mu_i} + (\frac{L\gamma}{\pi})^2} \; \frac{G\lambda(\lambda - a)L^2}{\pi^3} \tag{91}$$

A differential equation is obtained from Eqn. 86 by using the substitution

$$\sum_{m} b_m \sin(\frac{m\pi z}{L}) = f(z) \, . \tag{92}$$

Eqn. 86 is rewritten

$$R\,f''(z) + S\,f(z) = T\,\sinh(\lambda z)\,, \tag{93}$$

where $R = -\left(\frac{L}{m\pi}\right)^2 \left(m^2 - \frac{\left(\frac{L a}{m\pi}\right)^2}{\delta\,\lambda\mu_i} \right),$

$$S = \left(\frac{L\gamma}{\pi}\right)^2 , \tag{94}$$

$$T = \frac{G\,\lambda(\lambda\text{-}a)\,L^2}{\pi^2\ \sinh(\lambda L/\,2)}\ .$$

By using the boundary condition f(L/2) = 0 the solution for f(z) is obtained as a sum of a general solution and a particular solution:

$$f(z) = \frac{G\ \lambda(\lambda - a)\ \sinh \dfrac{\gamma z}{\sqrt{1 - \dfrac{\left(\frac{L a}{m\pi}\right)^2}{\delta\lambda\,\mu_i}}}}{\sinh \dfrac{\gamma \frac{L}{2}}{\sqrt{1 - \dfrac{\left(\frac{L a}{m\pi}\right)^2}{\delta\lambda\,\mu_i}}} \left[\ a^2 - \lambda^2 + \frac{\lambda}{\mu_i\,\delta}\ \left(1 + \left(\frac{L a}{m\pi}\right)^2\right)\right]}$$

$$- \frac{G\,\lambda(\lambda - a)\ \sinh(\lambda z)}{\left[\ a^2 - \lambda^2 + \frac{\lambda}{\mu_i\,\delta}\left(1 + \left(\frac{L a}{m\pi}\right)^2\right)\right]\ \sinh(\lambda L/2)}\ . \tag{95}$$

This can be simplified remarkably, when

$$\lambda^2 >> \frac{\lambda}{\mu_i\,\delta}\left(1 + \left(\frac{L a}{m\pi}\right)^2\right). \tag{96}$$

This yields

$$f(z) = \frac{G\lambda \ \sinh \dfrac{\gamma z}{\sqrt{1 - \dfrac{(\frac{La}{m\pi})^2}{\delta\lambda\,\mu_i}}}}{(a+\lambda)\ \sinh \dfrac{\gamma \ \frac{L}{2}}{\sqrt{1 - \dfrac{(\frac{La}{m\pi})^2}{\delta\lambda\,\mu_i}}}} - \frac{G\lambda \ \sinh(\lambda z)}{(a+\lambda)\ \sinh(\lambda L/2)} \ . \tag{97}$$

The solution is now substituted in Eqn. 81:

$$\sum_n \frac{na_n}{n^2 + (L\lambda/\pi)^2} \sin(n\pi z/L) = j\frac{\pi G}{L\lambda}\left(\frac{\lambda \ \sinh(\lambda z)}{(\lambda+a)\ \sinh(\lambda L/2)} + \right.$$

$$\left. \frac{a}{a+\lambda} \frac{\sinh \dfrac{\gamma z}{\sqrt{1 - \dfrac{(\frac{La}{m\pi})^2}{\delta\lambda\,\mu_i}}}}{\sinh \dfrac{\gamma \frac{L}{2}}{\sqrt{1 - \dfrac{(\frac{La}{m\pi})^2}{\delta\lambda\,\mu_i}}}}\right) . \tag{98}$$

Like b_m, a_n can also be solved by using the theory of Fourier-series. Eqn. 98 is multiplied by $\sin(\alpha \frac{\pi}{L} z)$ and integrated with respect to z in the range of $[-L/2, +L/2]$. This yields

$$a_n = Gj\frac{4}{\pi}(-1)^{\frac{n-1}{2}} \left\{ \frac{\lambda}{a+\lambda} \frac{\coth(\lambda L/2)}{n} + \frac{\gamma a}{\lambda(\lambda+a)}\left(1 - \frac{(\frac{La}{m\pi})^2}{\delta\lambda\,\mu_i}\right)^{-1/2} \right.$$

$$\left. \coth\left[\frac{1}{2}\gamma L\left(1 - \frac{(\frac{La}{m\pi})^2}{\delta\lambda\,\mu_i}\right)^{-1/2}\right] . \right.$$

$$\left.\frac{n^2+(L\lambda/\pi)^2}{n\left[n^2+\dfrac{(\frac{\gamma L}{\pi})^2}{1-\dfrac{(\frac{L a}{m\pi})^2}{\delta\lambda\,\mu_i}}\right]}\right\} \tag{99}$$

Equations 91 and 99 for b_m and a_n respectively can be greatly simplified by using equation 61 and the following inequality

$$\left|\frac{(\frac{La}{\pi})^2}{\delta\lambda\mu_i}\right| << 1\,. \tag{100}$$

This yields

$$a_n = Gj\frac{4}{\pi}(-1)^{\frac{n-1}{2}}\left[\frac{\coth(\lambda L/2)}{n}+\frac{\gamma a}{\lambda^2}\coth\left(\frac{1}{2}\gamma L\right)\right.$$

$$\left.\frac{n^2+(\lambda L/\pi)^2}{n(n^2+(\frac{\gamma L}{\pi})^2)}\right]\,, \tag{101}$$

$$b_m = G\left(\frac{L\lambda}{\pi}\right)^2(-1)^{\frac{m}{2}-1}\frac{4m}{\pi(m^2+(\gamma L/\pi)^2)(m^2+(\lambda L/\pi)^2)}\,. \tag{102}$$

3.6 The complete solution for rotor fields

Equations 64...69 together with equations 97...102 give simplified equations for $\overline{A}$ and $\overline{B}$ in closed form with respect to the complex constant G. This solution is of the same form as the solution by Yee (1971):

$$\overline{A}_x = G\left[e^{\lambda y}\frac{\sinh(\gamma z)}{\sinh(\gamma\frac{L}{2})}+(e^{ay}-e^{\lambda y})\cdot\frac{\sinh(\lambda z)}{\sinh(\lambda\frac{L}{2})}\right]e^{j(ax+s\omega_s t)}\,, \tag{103}$$

$$\overline{A}_y = j\,G(e^{\lambda y} - e^{ay})\frac{\sinh(\lambda z)}{\sinh(\lambda L/2)}\,e^{j(ax+s\omega_s t)}\,, \tag{104}$$

$$\overline{A}_z = j\,Ge^{\lambda y}\left[\ \coth(\lambda L/2) + \frac{a}{\gamma}\coth(\gamma L/2) - \right.$$

$$\left.\frac{a}{\gamma}\,\frac{\cosh(\gamma z)}{\sinh(\gamma\,L/2)}\right]\ e^{j(ax+s\omega_s t)}\,, \tag{105}$$

$$\overline{B}_x = j\,G\,\lambda\left\{\ e^{\lambda y}\left[\ \coth(\lambda\tfrac{L}{2}) + \frac{a}{\gamma}\coth(\gamma\tfrac{L}{2}) - \frac{a}{\gamma}\,\frac{\cosh(\gamma z)}{\sinh(\gamma\,L/2)}\right]\right.$$

$$\left. + (e^{ay} - e^{\lambda y})\frac{\cosh(\lambda z)}{\sinh(\lambda\,L/2)}\right\}\ e^{j(ax+s\omega_s t)}\,, \tag{106}$$

$$\overline{B}_y = a\,G\left\{\ e^{\lambda y}\left[\ \coth(\lambda\tfrac{L}{2}) + \frac{a}{\gamma}\coth(\gamma\tfrac{L}{2}) + \right.\right.$$

$$\left. + (\frac{\gamma}{a} - \frac{a}{\gamma})\frac{\cosh(\gamma z)}{\sinh(\gamma\,L/2)}\right]$$

$$\left. + \frac{\lambda}{a}(e^{ay} - e^{\lambda y})\frac{\cosh(\lambda z)}{\sinh(\lambda\,L/2)}\right\}\ e^{j(ax+s\omega_s t)}\,, \tag{107}$$

$$\overline{B}_z = -\lambda\,e^{\lambda y}G\left[\ \frac{\sinh(\gamma z)}{\sinh(\gamma\,L/2)} - \frac{\sinh(\lambda z)}{\sinh(\lambda\ L/2)}\right]\ e^{j(ax+s\omega_s t)}\,. \tag{108}$$

It can be seen from the result given for $\overline{A}_z$ that $\overline{A}_z$ $(z = \pm\ L/2) \neq 0$ contrary to the stipulated boundary conditions. This is a result of the approximations used, and does not detract from the value of the results. This implies that $\overline{A}_z$ and $\overline{B}_z$ decrease sharply to zero at the ends of the rotor over a small axial length of the rotor. By substituting the results of Eqns. 103...108 into the original differential equations, it is obvious that the error caused by the approximations is negligible except at points in the rotor less than a skin depth from both the air gap and the rotor ends, provided that Eqns. 61 and 100 hold.

3.6.1 The solution for constant G

The Equation 74 was derived by the aid of Ampère's circuital law; G can now be solved with Eqns. 74 and 7, when solutions for $\overline{H}_x$ and $\overline{H}_y$ are known in closed form. By substituting $\overline{H}_x$ and $\partial\overline{B}_y/\partial x$, Eqn. 79 can be written

$$\overline{K}_z = G\,j\left[\coth\left(\lambda\frac{L}{2}\right)\left(\frac{\lambda}{\mu_0\mu_i}+\frac{a^2\delta}{\mu_0}\right)+\left(\frac{\lambda a}{\mu_i\,\mu_0\gamma}+\frac{a^3\delta}{\mu_0\gamma}\right)\coth\left(\gamma\frac{L}{2}\right)\right.$$

$$\left.+\left(\frac{\gamma a\delta}{\mu_0}-\frac{a^3\delta}{\mu_0\gamma}-\frac{a\lambda}{\mu_0\mu_i\gamma}\right)\frac{\cosh(\gamma z)}{\sinh(\gamma\,L/2)}\right]\ . \tag{109}$$

When negligible terms are left out, the solution for G is found

$$G=\frac{-j\;\hat{I}\,K_0\mu_0}{\left(a^2\delta+\frac{\lambda}{\mu_i}\right)\left[\coth\left(\lambda\;\frac{L}{2}\right)+\frac{a}{\gamma}\coth\left(\gamma\frac{L}{2}\right)\right]}\ . \tag{110}$$

Two other quantities of interest are the fluxes $\overline{\Phi}_x$ and $\overline{\Phi}_z$ in the rotor per unit width. These fluxes are found by integrating the respective flux densities.

$$\overline{\Phi}_x=\int_{-\infty}^{0}\overline{B}_x\;dy\,,\;=jG\left[\coth(\lambda\,L/2)+\frac{a}{\gamma}\coth(\gamma L/2)-\frac{a}{\gamma}\frac{\cosh(\gamma z)}{\sinh(\gamma\,L/2)}\right.$$

$$\left.+\frac{\lambda}{a}\left[\frac{\cosh(\lambda z)}{\sinh(\lambda\,L/2)}\right]\right]e^{j(ax+s\omega_s t)}\,, \tag{111}$$

$$\overline{\Phi}_z=\int_{-\infty}^{0}\overline{B}_z\;dy\,,\;=G\left(\frac{\sinh(\gamma z)}{\sinh(\gamma\,L/2)}-\frac{\sinh(\lambda z)}{\sinh(\lambda\;L/2)}\right)e^{j(ax+s\omega\,_s t)}\ . \tag{112}$$

The quantitative nature of some vectors in Eqns. 103...108, 111 and 112 is sketched in Fig. 3. The quantities are shown at the rotor surfaces with respect to z. $\overline{A}_z$, as shown in Fig. 3, is not zero at the ends of the rotor, as was required by the boundary conditions. This is a result of the approximations made to obtain the solutions. A likely form of the actual distribution is shown by the dotted line in the Fig. 3.

Equations 108...113 indicate that all the eddy currents are concentrated close to the rotor surfaces at the air gap rotor interface and the endfaces. At the rotor surface in the middle of the rotor, the axial component of the eddy current has a maximum and is the only component present.

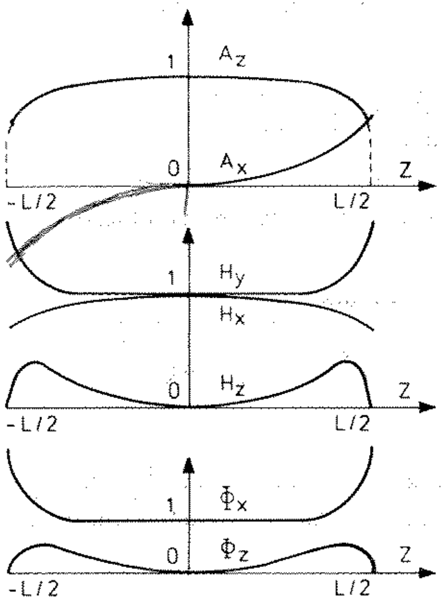

Figure 3. Approximate quantities at the surface of the rotor at standstill normalised with respect to values at the midpoint of the rotor.

The axial component decreases gradually towards the ends of the rotor. While the axial component decreases, the currents flowing in a circumferential direction near the rotor-air gap interface increase. The axial currents decrease sharply to zero close to the ends of the rotor which corresponds to currents penetrating radially into the rotor near the endfaces. The eddy currents of a two-pole machine are sketched in Fig. 4.

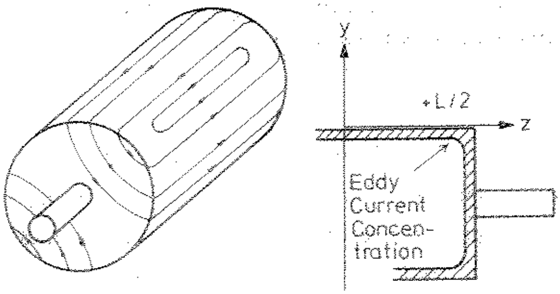

Figure 4. Approximate sketch of eddy currents of a two-pole machine.

The flux density distribution is related to the eddy current distribution. The tangential flux is concentrated near the ends of the rotor, corresponding to the deeply penetrating component of eddy current. There is a substantial axial component of flux corresponding to the tangential flow of currents. The resulting air gap flux density is greatest at the ends of the rotor.

3.7 Equivalent-circuit impedances.

Flux is the surface integral of the flux density

$$\overline{\Phi}_y = \int_{-\frac{L}{2}}^{\frac{L}{2}} \int_{-\frac{\tau}{2}}^{\frac{\tau}{2}} \overline{B}_y \,(y=0)dx\, dz\,. \qquad (113)$$

The induced electromotive force is calculated by the induction law of Faraday $\overline{E} = -d\overline{\Phi}/dt$. Integrating the flux $\overline{\Phi}_y$ (Eqn. 113) and differentiating with respect to time, the air gap voltage of the machine is found per stator turn. The air gap impedance is found by multiplying the air gap voltage by the effective stator turns and then dividing by the stator current:

$$\overline{Z}_\delta = \frac{2}{m}\, p\pi \,\frac{\mu_0\, K_0^2}{a^2}\, L\omega_s j \,\frac{1}{a\delta + \frac{\lambda}{a\,\mu_i}} \left\{ 1 + \frac{\frac{2}{aL}\left(1 - \frac{a^2}{\gamma^2} \right)}{\coth(\lambda\, L/2) + \frac{a}{\gamma}\, \coth(\gamma\, L/2)} \right\} . \qquad (114)$$

If the air gap impedance is calculated by assuming the machine to be infinitely long (Yee, 1971), we get

$$\overline{Z}'_\delta = \frac{2}{m}\, p\pi \,\frac{\mu_0\, K_0^2}{a^2}\, L\omega_s j \,\frac{1}{a\delta + \frac{\lambda}{a\mu_i}} \,. \qquad (115)$$

Thus a finite-length factor $F_g(s)$ may be defined by which the air gap impedance must be multiplied to account for the effect of finite rotor length:

$$\overline{F}_g(s) = \overline{Z}_\delta/\overline{Z}'_\delta = 1 + \frac{\frac{2}{aL}\left(1 - \frac{a^2}{\gamma^2}\right)}{\coth(\lambda L/2) + \frac{a}{\gamma}\coth(\gamma L/2)} \quad . \tag{116}$$

The following interesting properties of $\overline{F}_g(s)$ are noticed: When $s = 0$, $\overline{F}_g(s) = 1$. This is intuitively understandable: when there is no slip there are no eddy currents and the length of the rotor has no effect on the factor. $\left|\overline{F}_g(s)\right|$ increases monotonically with slip:

$$\lim_{s \to \infty} \left|\overline{F}_g(s)\right| = 1 + \frac{2}{aL} \ . \tag{117}$$

In general, $F_g(\infty)$ is not negligible. For small induction motors, it may be greater than 2; a typical value for a large turbogenerator is about 1.2. Eqn. 116 may then be used to estimate the effect of finite length. The air gap impedance $\overline{Z}_\delta$ is easily found to be equivalent to parallel impedances $\overline{Z}_m$ and $\overline{Z}'_r$

$$\overline{Z}_m = \frac{2}{m}\, p\pi \frac{\mu_0 K_0^2}{a^2} L\omega_s j \frac{1}{a\delta} \ , \tag{118}$$

$$\overline{Z}_r' = \frac{2}{m}\, p\pi \frac{\mu_0 K_0^2}{a^2} L\omega_s j \frac{a\mu_i}{\lambda} \left[1 + \frac{\frac{2}{aL}}{\coth(\lambda L/2) + \frac{a}{\gamma}\coth(\gamma L/2) - \frac{2a}{L\gamma^2}} \right] \quad . \tag{119}$$

$\overline{Z}_m$ is the usual magnetization impedance and $\overline{Z}'_r$ is the rotor impedance of an infinitely long machine multiplied by

$$\overline{F}_r(s) = 1 + \frac{\frac{2}{aL}}{\coth(\lambda L/2) + \frac{a}{\gamma}\coth(\gamma L/2) - \frac{2a}{L\gamma^2}} \quad . \tag{120}$$

When examining the absolute value and the phase angle of factor $\overline{F}_r(s)$, it is noticable that they are quite insensitive to changes in the permeability and the slip of the rotor. Thus $\overline{F}_r$ is almost a real constant depending only on machine dimensions.

In Eqns. 118 and 119 the components of air gap impedance - the magnetization impedance and the rotor impedance - are presented. By knowing the stator resistance and the leakage inductance, it is possible to form the equivalent circuit for the solid rotor induction machine, Fig. 5.

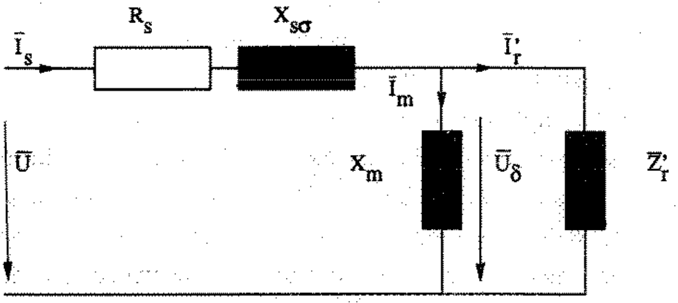

Figure 5. The equivalent circuit for the fundamental of the solid-rotor-induction-machine representing stator resistance R_s, stator leakage reactance $X_{s\sigma}$, magnetizing reactance X_m and rotor impedance $\bar{Z}_r$. The phase voltage is given as $\bar{U}$ and the air gap voltage as $\bar{U}_\delta$ Stator, rotor and magnetizing currents are $\bar{I}_s$, $\bar{I}'_r$ and $\bar{I}_m$ respectively.

4 THE EFFECTS OF SATURATION

4.1 Saturation and finite-length effects in solid-rotor induction machines

In the previous chapter the three dimensional solution for electromagnetic fields in a solid rotor under constant permeability was found. The constant phase angle of the rotor impedance, given by the linear theory as 45^o is contrary to many experimental results, which have invariably shown that the phase angle of unlaminated rotors is less than 45^o.

An important feature of solid-rotor induction machines is that the magnetic field strength at the surface of the rotor is usually sufficiently high to drive the rotor well into magnetic saturation. The limiting nonlinear theory (MacLean 1954), (Agarwal 1959), (Kesavamurthy, Rajagopalan 1959), (Angst 1962), (Chalmers 1962), (Jamieson 1968), (Rajagopalan, Balarama Murty 1969), (Krishnamurthy, Veluchamy 1972), (Yee, Wilson 1972), (Liese 1979), (Riepe 1981a) of flux penetration into solid rotor material considers that the flux density within the material may exist only at a magnitude equal to a saturation level B_s. This rectangular approximation to the B-H-curve is good only at high levels of magnetization. When the applied magnetizing force is assumed to be sinusoidally distributed, the rotor phase angle is given by this analysis as 26.6° (MacLean 1954), (Chalmers, Woolley 1972), (Yee, Wilson 1972). Using either the linear theory or the limiting nonlinear theory always gives a constant power factor for the rotor impedance independent of the slip, current or rotor material. This, however, is contrary to experimental results. In practice the phase angle of the rotor impedance is somewhere between these two extremes given by the linear theory and the limiting nonlinear theory.

Another method to determine the impedance of a solid rotor is to use a nonlinear function for the B-H-curve. The nonlinear variation of the fundamental B_1-H-curve is included in its entirety by substituting the equation $B_1 = CH^{(1-2/n)}$ (C and n are constants), which fits the magnetization curve quite well. This form was used by Pillai (1969) as a power-law approximation to the B_1-H-curve when H varies sinusoidally. He concluded that the rotor phase angle φ which is given by $\cos\varphi = (n/(2n-1))^{0.5}$ is virtually constant, independent of the slip but varying according to the exponent of H, lying between 35.3° when $n = 2$ and 45° when $n = \infty$. Test results show that the real phase angle of the rotor impedance approaches Pillai's value for proper value of n when slip increases and the surface of the rotor is driven into magnetic saturation. At a very low slip the phase angle approaches 45°. So the varying range of the phase angle is restricted between Pillai's value and 45°.

Louis A. Pipes (1956) presented a mathematical technique for determining the magnetic and electric field intensities and the current density in plane conducting metal plates of constant permeability produced by an external impressed alternating magnetic field. The fundamental Maxwell field equations are used as the basis of the analysis and expressions for the amplitudes of fields and currents are written in matrix form.

This method was later generalised by Greig and Freeman (1967). They calculated the electromagnetic travelling fields in electrical machines. The generalised structure considered comprises a number of laminar regions of infinite extent in the plane of lamination and of arbitrary thickness. The travelling field is produced by applied current sheet at the interface between two layers, distributed sinusoidally along the plane of lamination and flowing normally to the direction of the motion. The use of a transfer matrix provides the facility to introduce numerical values directly into the matrix formulation.

This technique has later been further developed by Freeman (1968) who published later (1974) a new version of the technique in polar co-ordinates. Polar co-ordinate representation was also used by Riepe (1981b). Cartesian co-ordinates in multi-layer representation have been used by Yamada (1970), Chalmers and Hamdi (1982) and Bergmann (1982). This technique gives fairly good results for the impedance of smooth infinitely long rotors and can be used for calculation of the stator, too.

The problem of end effects in solid rotors presents an indisputable difficulty. Several authors have not taken these effects into consideration at all. This is perhaps justifiable if the rotor is equipped with thick end rings of very low impedance that make the current paths as nearly axial. Kesavamurthy and Rajagopalan (1959) introduced an empirical factor to modify the value of ρ, the resistivity of rotor material, to incorporate the correction for end effects. They found it possible to get a close agreement between predicted and experimental results. There is, however, no information given how the empiral factor for end effect correction was arrived at.

Angst (1962) proposes a complex correction factor that is applicable to the effective rotor impedance. Deriving the factor involves the solution of the three dimensional field problem under constant permeability. Yee (1971) also solves the three dimensional field problem under constant permeability. This kind of an approach implies considerable axial variation in the air gap flux density (see Fig. 3.), and this is limited usually in practice, because of saturation in the stator teeth and rotor end areas (Woolley, Chalmers 1973). This assumption is, however, not quite valid in this case since the maximum flux density of high speed machines is normally limited to considerably lower values than in 50 Hz machines in order to avoid excessive iron losses in the stator (for example the maximum stator tooth flux density at no-load condition is about 1 T at nominal voltage of the 400 Hz test machine used in this work).

The present work also initially separates the two phenomena discussed in this chapter. An assumption is made that the rotor can be devided into saturated and unsaturated parts so that the behaviour of the rotor can be predicted using the three dimensional solution represented in the previous chapter together with the non-linear multi-layer method. This kind of an approach cannot be avoided unless a fully numerical three dimensional solution is used. A three dimensional analytical solution of Maxwell's equations for the overall non-linear problem is virtually impossible.

4.2 Electromagnetic fields in the saturated rotor of finite-length

The equations for rotor fields in closed form in a linear case were presented in Chapter 3. The qualitative nature of the field distribution in a finite length rotor is illustrated in Fig. 6. It is assumed that the flux Φ of the machine can be divided into two components. Flux Φ_1 enters the rotor at the air gap and follows a circumferential path near the air gap. Flux Φ_2 enters the rotor at the air gap and follows an axial path near the air gap and then a path across the endfaces. Φ_1 corresponds to the axial eddy currents, and Φ_2 to the end currents.

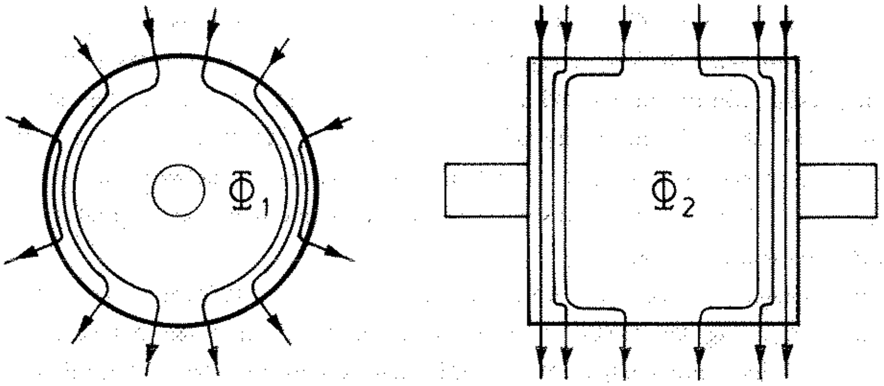

(a) (b)

Figure 6. The components of flux in a two-pole rotor. Φ_1 (a) corresponds to the axial eddy currents, and Φ_2 (b) to the end currents. Stator stack and the effective area of the rotor are of equal length.

Equations 103...108 show that the tangential magnetizing force $\overline{H}_x$ has a maximum at the midpoint of the rotor and diminishes towards the endfaces (see Figure 3.) Φ_1 is associated with the most heavily saturated parts of the rotor, while Φ_2 follows an unsaturated path in the rotor, when the machine is rotating at its normal working range of slip.

The aim of the following analysis is to derive the rotor impedance for a partly saturated rotor by using a multi-layer transfer-matrix method to describe the electromagnetic fields associated with Φ_1, and by using the linear theory to describe the fields associated with Φ_2.

4.3 Multi-layer transfer-matrix method

The multi-layer transfer-matrix method has been developed by several authors as was mentioned in section 4.1. In this method the machine is divided into numerous laminar regions of infinite extent. Fig. 7 presents the general multi-layer model and the co-ordinate system.

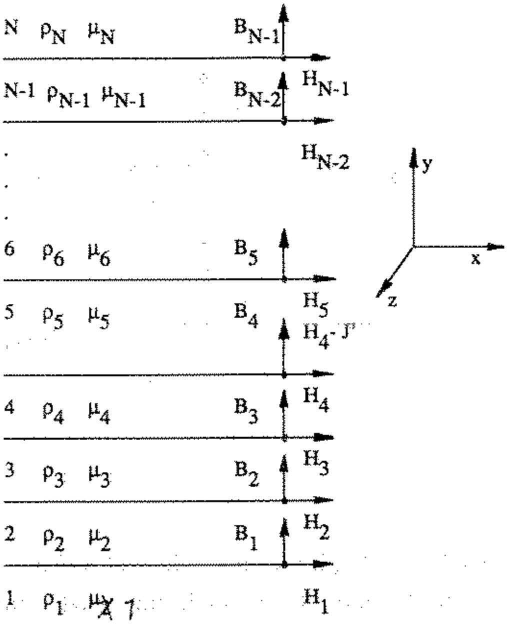

Figure 7. General multi-layer model with current sheet on boundary 4-5.

Even though the origin is now situated at a different point, the directions of the co-ordinate axes are the same as in Fig. 1. Also in this study the curvature of the rotor is neglected. Additionally the layers are assumed to be infinitely large since the end effects are not yet examined.

This multi-layer problem may be stated, with reference to Fig. 7, as follows. In a general sense, a current sheet $J = \mathrm{Re}\ \{J' \exp j(ax + \omega_s t)\}$ lies between two layers. Regions 1...N are layers of material with resistivity ρ_n and relative permeability μ_n. The problem is to determine the field distribution in all regions, and hence, if required, the power loss in and forces acting on any region.

A stationary reference frame is chosen in which the exciting field travels with velocity ω_s/a (m/s). Region n, in which the angular frequency is $\omega_n = s_n \omega_s$, is therefore travelling at velocity $(1 - s_n)\ \omega_s/a$ (m/s) relative to the stationary reference frame.

Consider a general region n, as in Fig. 8. The normal component of the magnetic flux density on the lower boundary is $\overline{B}_{n-1}$ and the tangential component of the magnetic field strength is $\overline{H}_{n-1}$. The corresponding values at the upper boundary are $\overline{B}_n$ and $\overline{H}_n$, respectively. The field in the region varies everywhere as $\mathrm{Re}\ \{\exp j(ax + \omega_n t)\}$.

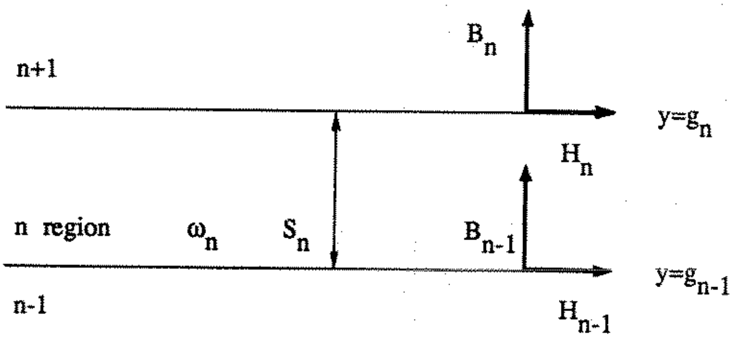

Figure 8. General region n.

The general region is assumed to be planar, and all end effects are neglected, as is magnetic saturation. Displacement currents in the conducting media are also assumed to be negligible. The current sheet varies sinusoidally in the x-direction and with time; it is of infinite extent in the x-direction, and infinitesimally thin in the y-direction. The necessary boundary conditions may be written as follows:

a) $\overline{B}_y$ is continuous across a boundary.
b) All field components disappear at $y = \pm \infty$.
c) If a current sheet exists between two regions, then $\overline{H}'_n = \overline{H}_{n-1} - \overline{J}'$, where $\overline{H}'_n$ is the magnetizing force immediately above the current sheet and $\overline{H}_{n-1}$ is the magnetizing force immediately-below the current sheet.

Maxwell's Equations 9 and Eqn. 11 give the following analogously with Eqn. 15

PROC IEE, Vol 115, No 12 Dec 1968
pp 1772 .. 1776

Freeman [illegible] permeabilit[illegible] [illegible] on [illegible] (x-[illegible], y-[illegible])

$$\frac{\partial^2 \overline{B}_y}{\partial y^2} = \overline{B}_y(a^2 + j\omega_{\underset{s}{\cancel{n}}}\mu_0\mu_n\sigma_n s)\,, \qquad (121)$$

$$\bar{\Theta}_n = (a^2 \mu_{x,n}/\mu_{y,n} + j\mu_0\mu_{x,n}\omega_s s_n \sigma_n)^{1/2}$$

the following annotation is used

$$\overline{\Theta}_n = (a^2 + j\omega_{\underset{s}{\cancel{n}}}\mu_0\mu_n\sigma_n s)^{1/2} = (a^2 + \frac{j}{d_n^2})^{1/2}\,, \qquad (122)$$

where d_n is the depth of penetration in region n

For region n, when n = N or 1, the solution to Eqn. 121 may be written

$$\overline{B}_y = (\, A \cosh(\overline{\Theta}_n y) + C \sinh(\overline{\Theta}_n y)\,)\, e^{j(ax+\omega_n t)}, \tag{123}$$

where constants A and C are to be found from the boundary conditions. Since the divergence of $\overline{B}$ is zero and $\overline{B}_z = 0$ in a region, $\overline{H}_x$ can be solved. These give

$$\frac{\partial \overline{B}_y}{\partial y} = \overline{\Theta}_n(\, A \sinh(\overline{\Theta}_n y) + C \cosh(\overline{\Theta}_n y)\,)e^{j(ax+\omega_n t)} = -\frac{\partial \overline{B}_x}{\partial x} . \tag{124}$$

$\overline{H}_x$ is now found by integration:

$$\overline{H}_x = \frac{\overline{\Theta}_n}{ja\mu_0\mu_n}(\, A \sinh(\overline{\Theta}_n y) + C \cosh(\overline{\Theta}_n y)\,)e^{j(ax+\omega_n t)} . \tag{125}$$

The following annotation is used

$$\overline{\beta}_n = \frac{\overline{\Theta}_n}{ja\,\mu_0\mu_n} . \qquad = \frac{\Theta_n}{j a \mu_0 \mu_{x,n}} \tag{126}$$

Now, according to Greig and Freeman (1967), the following matrix equation may be written for region n , when $\overline{H}_x = \overline{H}_n$ and $\overline{B}_y = \overline{B}_n$.

$$\begin{bmatrix} \overline{B}_n \\ \overline{H}_n \end{bmatrix} = \begin{bmatrix} \cosh(\overline{\Theta}_n S_n) & \frac{1}{\overline{\beta}_n} \sinh(\overline{\Theta}_n S_n) \\ \overline{\beta}_n \sinh(\overline{\Theta}_n S_n) & \cosh(\overline{\Theta}_n S_n) \end{bmatrix} \begin{bmatrix} \overline{B}_{n-1} \\ \overline{H}_{n-1} \end{bmatrix} = [T_n] \begin{bmatrix} \overline{B}_{n-1} \\ \overline{H}_{n-1} \end{bmatrix} \tag{127}$$

The matrix $[T_n]$, following Pipes (1956) is called the transfer-matrix for region n. Also solving for the field in the top region on the boundary g_N

$$\overline{H}_{N-1} = -\overline{\beta}_N \overline{B}_{N-1} . \tag{128}$$

In the top region N the magnetic field density and the magnetic field strength must diminish gradually to zero according to boundary condition (b). So

$$\overline{B}_N = \overline{B}_{N-1}\, e^{\overline{\Theta}_n (g_{N-1} - y)}, \tag{129}$$

$$\overline{H}_N = -\overline{\beta}_N\, \overline{B}_{N-1}\, e^{\overline{\Theta}_n (g_{N-1} - y)}. \tag{130}$$

Solving for the field in the bottom region on the boundary g_1:

$$\overline{H}_1 = \overline{\beta}_1\, \overline{B}_1 . \tag{131}$$

In region 1, where the magnetic field density must approach zero as y diminishes, it can be written:

$$\overline{B}_1 = \overline{B}_1\, e^{\overline{\Theta}_1 (y - g_1)}, \tag{132}$$

$$\overline{H}_1 = \overline{\beta}_1\, \overline{B}_1\, e^{\overline{\Theta}_1 (y - g_1)}. \tag{133}$$

The transfer-matrix may be used as follows, bearing in mind boundary conditions (a) and (c). The current sheet lies between regions r and r+1.

$$\begin{bmatrix} \overline{B}_r \\ \overline{H}_r \end{bmatrix} = \begin{bmatrix} T_r \end{bmatrix} \begin{bmatrix} T_{r-1} \end{bmatrix} \cdots \begin{bmatrix} T_2 \end{bmatrix} \begin{bmatrix} \overline{B}_1 \\ \overline{H}_1 \end{bmatrix}, \tag{134}$$

$$\begin{bmatrix} \overline{B}_{N-1} \\ \overline{H}_{N-1} \end{bmatrix} = \begin{bmatrix} T_{N-1} \end{bmatrix} \begin{bmatrix} T_{N-2} \end{bmatrix} \cdots \begin{bmatrix} T_{r+1} \end{bmatrix} \begin{bmatrix} \overline{B}_r \\ \overline{H}_r - \overline{J}' \end{bmatrix}. \tag{135}$$

The analysis above may be programmed to compute the electromagnetic fields and power flow at all boundaries when $\overline{B}_n$ or $\overline{H}_n$ is given at any boundary. In this work the computing is commenced by assuming a low value of tangential field $\overline{H}_1$ at the inner rotor surface and calculating the corresponding normal component of flux density $\overline{B}_1$ by using Eqn. 131. The transfer-matrix technique then evaluates $\overline{B}_n$ and $\overline{H}_n$ at all inter-layer boundaries up to the surface of the rotor. At this interface, where $\overline{H}_n$ corresponds to the total rotor current, the model is combined with a conventional equivalent-circuit representation of the air gap and stator. Iterative adjustment of $\overline{H}_1$ is made to adapt the conditions at the rotor surface.

To take into account the non-linear magnetization characteristic of any unlaminated steel layer, such a layer is represented by a number of thin sub-layers. The permeability of each sub-layer is taken as corresponding to the tangential magnetizing field strength in the preceding sub-layer. The B-H-curve of the different materials may be represented by 20 data points between which a linear approximation is used.

The general form of the Poynting vector is

$$\mathbf{S} = \mathbf{E} \times \mathbf{H} \ . \tag{136}$$

The Poynting vector in complex plane is

$$\overline{S} = \overline{E}_n \overline{H}_n^{\,*} \ . \tag{137}$$

The time-average power density in (W/m²) passing through a surface may be found by using one of the following two expressions;

a) $n = r, r+1...N-1$

$$P'_{in,n} = 0.5 \operatorname{Re}\left\{ \overline{E}_n \overline{H}_n^{\,*'} \right\} \tag{138}$$

where $\overline{H}_n^{\,*'} = \overline{H}_n^{\,*} - \overline{J}^{\,*'}$, when $n = r$ and $\overline{H}_n^{\,*'} = \overline{H}_n^{\,*}$, when $n = r+1...N-1$.

b) $n = 1, 2,...r$

$$P_{in,n} = -0.5 \operatorname{Re}\left\{ \overline{E}_n \overline{H}_n^{\,*} \right\} \tag{139}$$

In Eqns. 138 and 139 $\overline{E}_n$ is the component of electric field strength in the z-direction:

$$\overline{E}_n = -(\omega_n/a)\overline{B}_n \ . \tag{140}$$

The net power density into a region is the difference between the power density in and the power density out:

$$P_n = \mathrm{Re}\left\{ \frac{\omega_s}{2a} (\overline{B}_n \overline{H}_n^{*'} - \overline{B}_{n-1} \overline{H}_{n-1}^{*'}) \right\} \tag{141}$$

The mechanical power density developed by the region under slip s_n is

$$P_{mech} = P_n(1-s_n) \tag{142}$$

The I^2R loss developed by the region is

$$P_n - P_{mech} = s_n P_n \tag{143}$$

4.4 Determining of the fundamental permeability in a nonlinear material

A sinusoidally varying magnetic field strength $H = \hat{H}\sin\omega t$ creates a non-sinusoidal magnetic field density in a saturable material (Deleroi, Kovacs 1990). The amplitude spectrum of this field density can be numerically determined with the DC-magnetization curve of the material. In Fig. 9 it can be seen how the flattened B(ωt)-wave contains a fundamental amplitude which is remarkably higher than the real maximum value. In a pure power analysis the harmonics can be left out of the examination, because according to the Poynting vector, only waves with the same frequency create torque. So the saturation-dependent fundamental permeability of the material must be determined.

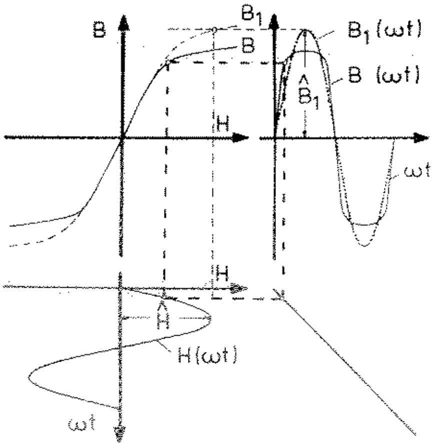

Figure 9. Determining the fundamental magnetic field density $B_1(\omega t)$ produced by an external impressed sinusoidally alternating magnetic field strength $H(\omega t)$ and the B_1-H-curve with DC-magnetization curve.

With reference to Fig. 9 the fundamental amplitude $\hat{B}_1$ of the Fourier-series of the field density B(ωt) is found by numerical integration:

$$\hat{B}_1 = \frac{2}{\pi}\int_0^{\pi} B(\omega t)\sin(\omega t)d\omega t\,. \tag{144}$$

The fundamental permeability of a particular working point is determined as

$$\mu_1(\hat{H}) = \hat{B}_1/\hat{H}. \tag{145}$$

4.5 The equivalent circuit impedance of the rotor

To be able to work out the equivalent circuit, the stator current component required to balance the magnetomotive force due to currents in the rotor solid iron must be known. These rotor currents can be examined with the rotor impedance referred to the stator. This impedance is determined by the ratio of the voltage $\overline{U}'_r$, which is induced in stator windings by the rotor flux, to the corresponding rotor current $\overline{I}'_r$ referred to the stator. When the flux distribution is known it is possible to determine the rotor impedance in a closed form. In Fig. 10 the stator windings have been presented between two infinite half spaces. The permeability of the stator laminations is assumed to be infinite, and the air gap δ is assumed to be zero so that the respective magnetomotive forces are left out of the examination. No mistake is made, because the effect of these magnetomotive forces can be calculated separately (Chapter 6). The stator windings carry currents I_{1U} , I_{1V} , I_{1W}.

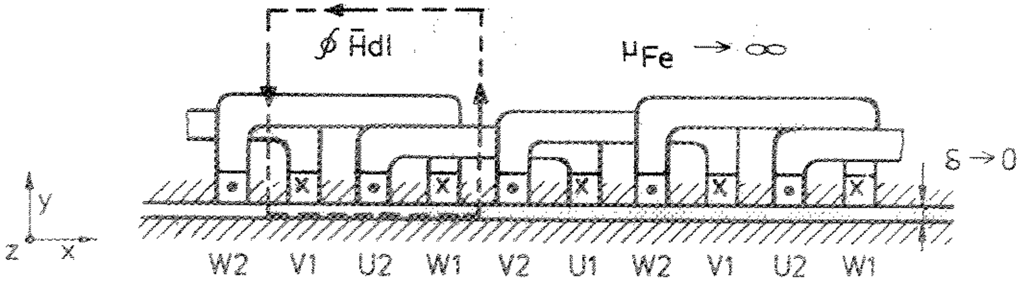

Figure 10. Stator windings and the integration path to calculate the rotor impedance.

According to Ampère's law (Eqn. 70) the line integral calculated following the contour of a surface is equal to the sum of currents which flow through the same surface. This law is applied to the integration path of Fig. 10 and only the fundamental of the current sheet is examined. The magnetomotive force is designated $\overline{\theta}$.

$$\overline{\theta} = \frac{4}{\pi}\,\frac{m}{2}\,\frac{N\xi}{p}\,\sqrt{2}\,\overline{I}'_r = \int_{-\tau_p}^{0} \overline{H}_{rx}\, e^{jax}\, dx\ , \tag{146}$$

where $\overline{H}_{rx}$ is the tangential magnetic field strength at the rotor surface and m the number of phases. $\overline{H}_{rx}$ is not a function of x, thus

$$\overline{\theta} = \int_{-\tau_p}^{0} \overline{H}_{rx}\, e^{jax}\, dx = \frac{2\,\overline{H}_{rx}}{ja}\ . \tag{147}$$

The rotor current referred to the stator is then

$$\overline{I}'_r = \frac{-\,j\,\pi p}{amN\xi\ \sqrt{2}}\,\overline{H}_{rx}\ . \tag{149}$$

The air gap flux of the machine is found by integrating the radial flux density at the rotor surface over a pole pitch. Faraday's induction law, gives an equation for the rotor voltage per phase referred to the stator:

$$\overline{U}'_r = -j\omega_s\,\frac{N\xi}{\sqrt{2}} \int_{-\frac{\tau_p}{2}}^{\frac{\tau_p}{2}} \overline{B}_{ry}\, e^{\,jax}\, L\, dx = -j\,\frac{2\omega_s N\xi L}{\sqrt{2}\ a}\,\overline{B}_{ry}\ . \tag{150}$$

Finally the rotor impedance referred to the stator is found:

$$\overline{Z}'_r = \frac{\overline{U}'_r}{\overline{I}'_r} = \frac{2\omega_s\,(N\xi)^2 mL}{\pi p}\ \frac{\overline{B}_{ry}}{\overline{H}_{rx}}\ . \tag{151}$$

5 CALCULATING A SATURABLE ROTOR OF FINITE LENGTH

5.1 Equivalent circuit for the fundamental

The equivalent circuit applicable to the steady state fundamental performance of an induction machine was shown in Fig. 5. In the present analysis the a priori assumption is made that the air gap and the rotor phenomena can be represented by separate branches of the equivalent circuit. This assumption is almost always made and seems to be reasonable for finite-length machine models, too. In the derivation of the equivalent circuit parameters, it is common to associate the load current $\overline{I}'_r$ with $\overline{H}_x(y=0)$ as was done in Chapter 4. Such a simple relationship does not hold here, since $\overline{H}_x(y=0)$ varies with axial position on the rotor surface. The equivalent circuit impedance is:

$$\overline{Z}'_r = \frac{\hat{U}^2_\delta \cdot m}{2\ \overline{S}'^*}, \tag{152}$$

where $\hat{U}_\delta$ is the peak stator-induced voltage,
m is the number of phases,
$\overline{S}'^*$ is the complex conjugate of the complex apparent power flow into the rotor.

5.2 Analysis of the rotor fields

Equations 103...108 give the rotor fields when a constant magnetic permeability is assumed. The equations are written with respect to rotor co-ordinates. The analysis proceeds from Eqns. 103...108 with the assumption that the tangential magnetic field strength at the rotor surfaces (y = 0 or z = ± L/2) is distributed in essentially the same way as when no saturation occurs. More explicitly, it is assumed that at any given slip s the distribution is described by the Eqns. 103...108 in terms of the parameter $\gamma(s)$.

Using the magnetic field strength as a boundary condition, the tangential electric field strength at the rotor surfaces and the flux per pole are determined. The Poynting vector at the rotor surface is then formed and the rotor impedance $\overline{Z}'_r$ determined using Eqn. 152.

Since the fields corresponding to $\overline{\Phi}_2$ (Fig. 6) are described using a constant relative permeability μ_i , $\overline{E}_x(y = 0)$, $\overline{E}_y$ (z = ±L/2) and $\overline{E}_x$ (z = ±L/2) are determined directly from Eqns. 103...108, as is $\overline{\Phi}_2$. $\overline{E}_z$ (y = 0) and $\overline{\Phi}_1$ are determined from $\overline{H}_x$(y = 0) assuming that the magnetic properties of the material can be described using the multi-layer transfer-matrix method deviding the rotor also in disks.

Using Eqns. 106...108 for flux densities also gives magnetic field strengths. The following modifications are made: 1) The fields are written with respect to stator co-ordinates. 2) Annotation $\overline{H}_0$ is used.

$$\overline{H}_0 = \frac{1}{\mu_0\mu_i} G\,|\lambda| \,. \tag{153}$$

It is also assumed that $|\lambda| >> a$ and $|\lambda| >> |\gamma|$. These assumptions give for $\overline{H}_x$ in rotor co-ordinates

$$\overline{H}_x\,(y=0) = \frac{1}{\mu_0\mu_i} jG\lambda e^{j(ax+s\omega_s t)}\left[\ \coth(\frac{\lambda L}{2}) + \frac{a}{\gamma}\coth(\frac{\gamma L}{2}) - \frac{a}{\gamma}\,\frac{\cos h(\gamma z)}{\sin h(\frac{\gamma L}{2})}\right] \,. \tag{154}$$

Eqn. 154 can be written in a new form after substitutions:

$$\overline{H}_x\,(y=0) = \frac{\hat{I}\,\frac{2\,\cdot\,m}{\pi p D}\,\xi\,N}{\frac{a^2\,\delta\,\mu_i}{\lambda} + 1}\left[\ 1 - \frac{\frac{a}{\gamma}\ \frac{\cos h(\gamma z)}{\sin h\,(\frac{\gamma L}{2})}}{\coth(\frac{\lambda L}{2})\underset{+}{\wedge}\frac{a}{\gamma}\ \coth(\frac{\gamma L}{2})}\right] , \tag{155}$$

where the term $2\hat{I}m\xi N/(\pi p D)$ is the magnetic field strength used for infinitely long machines (Agarwal, 1960), (Bergmann 1982) i.e. machines equipped with ideal end rings.

When it is noticed that the phase angle of the imaginary unit is $\pi/2$ and the phase angle of λ is $\pi/4$, Eqn. 154 using $\overline{H}_0$ and according to Eqn. 6 can be written in stator co-ordinates

$$\overline{H}_x\,(y=0) = \overline{H}_0\, e^{j\frac{3\pi}{4}}\, e^{j(ax_1+\omega_s t)}\left[\ \coth(\frac{\lambda L}{2}) + \frac{a}{\gamma}\coth(\frac{\gamma L}{2}) - \frac{a}{\gamma}\,\frac{\cos h(\gamma z)}{\sin h(\frac{\gamma L}{2})}\right] . \tag{156}$$

Respectively, it can be written

$$\overline{H}_z\,(y=0) = -\overline{H}_0\, e^{j\frac{\pi}{4}}\left[\ \frac{\sinh(\gamma z)}{\sinh(\gamma\,\frac{L}{2})} - \frac{\sinh(\lambda z)}{\sinh(\frac{\lambda L}{2})}\right] e^{j(ax_1+\omega_s t)} , \tag{157}$$

$$\overline{H}_x(z=\tfrac{L}{2}) = \overline{H}_0\, e^{j\frac{3\pi}{4}}\, e^{ay} \coth(\tfrac{\lambda L}{2})\, e^{j(ax_1+\omega_s t)}, \tag{158}$$

$$\overline{H}_y(z=\tfrac{L}{2}) = \overline{H}_0\, e^{j\frac{\pi}{4}}\, e^{ay}\, e^{j(ax_1+\omega_s t)}. \tag{159}$$

Similar equations also apply at the other end of the rotor ($z = -\frac{L}{2}$). Provided that σ is constant Eqns. 9b and 10a give

$$\overline{\mathbf{E}} = -\partial\overline{A}/\partial t \tag{160}$$

The electric field strength in the tangential direction at the rotor surface $\overline{E}_x(y=0)$, $\overline{E}_x(z=\pm L/2)$ and the normal component $\overline{E}_y(z=\pm L/2)$ are found by derivating Eqns. 103 and 104 and by substituting the values of y and z:

$$\overline{E}_x(y=0) = -\overline{H}_0 e^{j\frac{\pi}{2}} \sqrt{\omega_s\mu_0\mu_i\rho/s}\; e^{j(ax_1+\omega_s t)} \frac{\sinh(\gamma z)}{\sinh(\gamma\frac{L}{2})}, \tag{161}$$

$$\overline{E}_x(z=\tfrac{L}{2}) = -\overline{H}_0 e^{j\frac{\pi}{2}} \sqrt{\omega_s\mu_0\mu_i\rho/s}\; e^{ay}\, e^{j(ax_1+\omega_s t)}, \tag{162}$$

$$\overline{E}_y(z=\tfrac{L}{2}) = -\overline{H}_0 \sqrt{\omega_s\mu_0\mu_i\rho/s}\; e^{ay}\, e^{j(ax_1+\omega_s t)}. \tag{163}$$

Finally $\overline{E}_z$ ($y=0$) must be determined by using diskwise the nonlinear method presented in chapter 4 (Fig. 11). Eqn. 134 is written again by using the annotations for the normal component of flux density and the tangential component of magnetic field strength:

$$\begin{bmatrix}\overline{B}_{yr}\\ \overline{H}_{xr}\end{bmatrix} = \begin{bmatrix} T_r \end{bmatrix} \begin{bmatrix} T_{r-1} \end{bmatrix} \cdots \begin{bmatrix} T_2 \end{bmatrix} \begin{bmatrix}\overline{B}_{y1}\\ \overline{H}_{x1}\end{bmatrix}. \tag{164}$$

Eqn. 164 is programmed to compute the field quantities at the boundaries between all layers. The procedure starts by assuming a low value of tangential field strength $\overline{H}_{x1}$ deep in the rotor (Fig. 11). At the rotor surface the value $\overline{H}_{xr}$ is compared with the tangential field strength value of the linear theory (see Eqn. 155). The value of $\overline{H}_{x1}$ is iteratively changed until the field strengths at the rotor surface are equal.

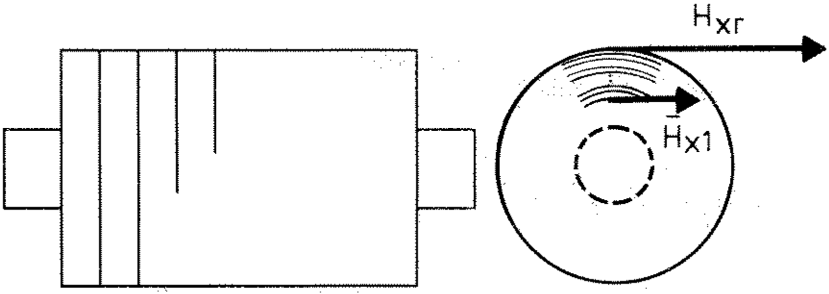

Figure 11. The rotor is divided into disks as well as into layers.

The electric field strength in z-direction at the surface of the rotor according to Eqn. 140 is

$$\overline{E}_z(y=0) = (s\omega_s/a)\,\overline{B}_{yr}\,. \tag{165}$$

$\overline{\Phi_2}$ can be obtained by integrating, over surface y=0, that component of $\overline{B}_y$ (y=0) which corresponds to the tangential electric field strength $\overline{E}_x$ (y=0). The curl equation of the electric field strength gives

$$\frac{\partial}{\partial x}\overline{E}_z - \frac{\partial}{\partial z}\overline{E}_x = \frac{\partial}{\partial t}\,\overline{B}_y\,. \tag{166}$$

By now choosing only the component that corresponds to the flux $\overline{\Phi}_2$ Eqns. 161 and 166 give

$$\overline{B}_{\Phi 2} = \int \frac{\partial \overline{E}}{\partial z}\,dt = \frac{1}{j\,\omega_s}\,\overline{H}_0\,e^{j\frac{\pi}{2}}\sqrt{\omega_s\mu_0\,\mu_i\,\rho/s}\;e^{j(ax_1+\omega_s t)}\,\gamma\,\frac{\cosh(\gamma z)}{\sinh(\gamma\,\frac{L}{2})}\,. \tag{167}$$

Integrating over surface y = 0 gives

$$\overline{\Phi}_2 = \int_{-\frac{\tau_p}{2}}^{\frac{\tau_p}{2}}\int_{-\frac{L}{2}}^{\frac{L}{2}} \overline{B}_{\Phi 2}\,dz\,dx = \frac{4}{\omega_s a}\,\overline{H}_0\sqrt{\omega_s\,\mu_0\,\mu_i\,\rho/s}\,. \tag{168}$$

$\overline{\Phi}_1$ is computed by using diskwise the multi-layer transfer-matrix method. The air gap voltage of the machine is calculated with Faraday's induction law

$$\overline{U}_\delta = -j\omega_s \frac{N\xi}{\sqrt{2}} \left(\overline{\Phi}_1 + \overline{\Phi}_2\right) . \tag{169}$$

The complex power that flows into the rotor is found by integrating the Poynting vector over the rotor surfaces:

$$\overline{S}' = \pi D \Bigg[-\int_{-L/2}^{+L/2} (1/2)\, \overline{E}_z(y=0)\, \overset{*}{\overline{H}_x}(y=0)\, dz + \int_{-L/2}^{+L/2} (1/2)\, \overline{E}_x(y=0)\, \overset{*}{\overline{H}_z}(y=0)\, dz$$

$$+\int_{-\infty}^{0} \overline{E}_y\, (z=L/2) \overset{*}{\overline{H}_x}(z=L/2)\, dy - \int_{-\infty}^{0} \overline{E}_x\, (z=L/2)\, \overset{*}{\overline{H}_y}\, (z=L/2)\, dy. \Bigg] \tag{170}$$

6 THE MAGNETIZING CURRENT OF THE SOLID-ROTOR INDUCTION MACHINE

The determine the magnetizing current of the machine the magnetomotive force of the magnetic path of the machine must be calculated. This magnetomotive forve (mmf) is the line integral of the magnetomotive forces in different parts of the machine. If the path of the heaviest induction is chosen the top value $\hat{V}_m$ of the mmf is found. With respect to Fig. 12 and assuming the two air gaps to be identical the magnetomotive force of the machine is

$$\hat{V} = 2\hat{V}_\delta + \hat{V}_r + \hat{V}_s = \int_C H \cdot dl = 2\int_{C_\delta} H \cdot dl + \int_{C_r} H \cdot dl + \int_{C_s} H \cdot dl \;, \tag{170}$$

where the subscripts are; δ for air gap, r for rotor, s for stator.

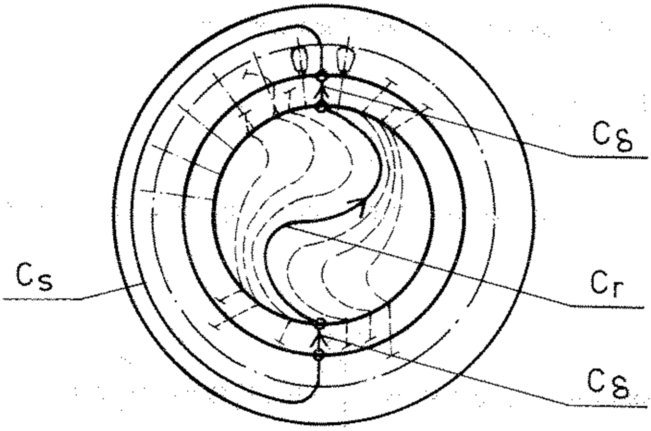

Figure 12. The integration path of the magnetomotive force.

In chapter 5 the method to calculate the rotor impedance $\overline{Z}'_r$ was presented. This impedance contains all effects of the fundamental waves in the rotor including the magnetizing of the rotor material. An assumption is made that the air gap and rotor phenomena can be represented by separate branches of the equivalent circuit (Fig. 5). The magnetizing reactance X_m of the equivalent circuit then contains the effects of the stator laminations and the air gap only.

The top value of the magnetomotive force created by a current I_m in an m-phase stator winding is

$$\hat{V}_m = \frac{m}{2}\,\frac{4}{\pi}\,\frac{\xi N}{2p}\,\sqrt{2}\,I_m \tag{172}$$

The magnetomotive force is so distributed in the air gap that both positive and negative values of the amplitude $\hat{V}_m$ affect during the same time on the integration path. Thus the effective value of the magnetizing current I_m that corresponds to the air gap and stator phenomena is

$$I_m = \frac{2\,\hat{V}_\delta + \hat{V}_s}{m\,\frac{4}{\pi}\,\frac{\xi N}{2p}\,\sqrt{2}} \tag{173}$$

This gives an opportunity to determine the magnetizing reactance X_m of Fig. 5 as a ratio between the air gap voltage U_δ and the current I_m

$$X_m = \frac{U_\delta}{I_m} \; . \tag{174}$$

7. TORQUES DUE TO HARMONICS

In addition to the fundamental the stator slots and windings create harmonic magnetomotive forces in the air gap. The harmonic mmfs rotate in opposite directions at different speeds. The frequencies of the eddy currents induced by the harmonic mmfs are high and the depths of penetration are small. The harmonics generate remarkable losses in a solid rotor. The effects of these harmonics in asynchronous motors have been examined for instance by Agarwal (1960), Boller and Jordan (1963), Jordan and Taegen (1965), Jordan and Raube (1972) and Bergmann (1982).

On the rotor surface several alternating excitations of differing frequencies are superimposed. The effects of the fundamental can reliably be calculated by determining the fundamental permeability μ_1 as was explained in section 4.4, but the excitation on the surface of the rotor varies in such a complicated manner that great difficulties arise when trying to determine the permeabilities for the numerous harmonics.

Usually just one incremental permeability μ_r is used for all harmonic mmfs. For example Bergmann (1982) has used the value $\mu_r = 40\ \mu_0$ to describe the behaviour of all the harmonics in a solid rotor made of ST60-steel. Chalmers et. al. (1980) have reported some basic measurements of the incremental permeability of steel under conditions where two alternating excitations were superimposed. A thin ring of "mild steel" was separately excited with two coils. The incremental permeability with an AC-signal superimposed on a steady field ($H_{DC} > 60$ A/cm) varied in the range of $\mu_r = 25\ \mu_0 ... 55\ \mu_0$ depending on the values of the AC-flux density so that the highest values of the AC-flux density (B_{AC} = 0,4 T) gave the highest incremental permeability.

When the test was repeated to get results for AC-incremental permeability over a range of low frequency RMS magnetizing force H_{lf}, μ_r was found to vary in the range of μ_r = 200 $\mu_0 ... 40\ \mu_0$ (0 A/cm < H_{lf} < 160 A/cm) depending mainly on the magnetizing force of the AC signal so that the highest value H_{AC} = 40 A/cm gave the lowest incremental permeability of $\mu_r = 40\ \mu_0$ at H_{lf} = 160 A/cm. The tendency to get even lower values of permeability ($\mu \approx 12\ \mu_0$) at higher values of H_{lf} > 160 A/cm was also seen.

7.1 Winding harmonics

The travelling velocity of the fundamental on the stator surface is faster than the velocities of the harmonics. The ordinal of the stator harmonic ν for an m-phase stator winding is given by (Richter 1954):

$$\nu = 2 g_1 m + 1 \tag{175}$$

where g_1 is an arbitrary positive or negative integer and m is the number of phases. If ν is positive, the harmonic is rotating in the same direction as the fundamental, and in the opposite direction if ν is negative. The angular velocity of the harmonic with respect to the stator is

$$\omega_{\nu s} = \frac{\omega_s}{\nu} \ . \tag{176}$$

The harmonic field induces a fundamental voltage into the stator. The order of the harmonic thus implies the amount of wavelengths per one pair of fundamental poles $2\tau_p$. The number of pole pairs and the pole pitch of the harmonic are thus

$$p_\nu = \nu p \,, \tag{177}$$

$$\tau_\nu = \frac{\tau_p}{\nu} \ . \tag{178}$$

The amplitude of the ν:th harmonic mmf expressed with the fundamental amplitude $\hat{V}_1$ and the winding factors ξ_1 and ξ_ν for the fundamental and the ν:th harmonic respectively- is

$$\hat{V}_\nu = \hat{V}_1 \frac{\xi_\nu}{\nu\, \xi_1} \,, \tag{179}$$

where $$\xi_\nu = \frac{2 \sin\left(\nu \frac{W}{\tau_p} \frac{\pi}{2}\right) \sin\left(\frac{\nu}{m} \frac{\pi}{2}\right)}{\frac{Q_s}{mp} \sin\left(\nu\pi \frac{p}{Q_s}\right)} \ . \tag{180}$$

Here w/τ_p is the ratio between the coil pitch and the pole pitch of the stator winding and Q_s is the number of stator slots. The slip of the rotor with respect to the ν:th stator harmonic is

$$s_\nu = 1-\nu(1 - s) . \qquad (181)$$

The angular velocity of the ν:th harmonic in the rotor is thus

$$\omega_{\nu r} = \omega_s (1 - \nu (1 - s)) . \qquad (182)$$

The effects of the harmonics can be studied with the help of the equivalent circuit given in Fig. 13 (Richter 1954).

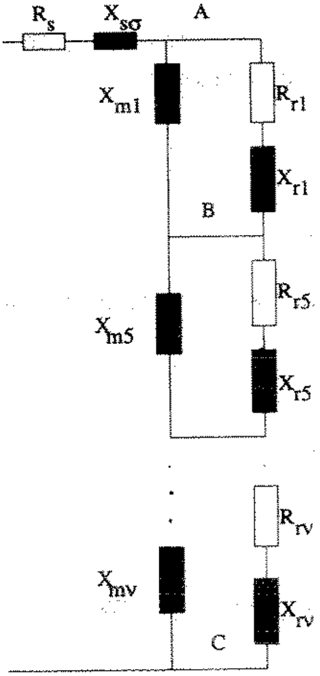

Figure 13. Simplified complete equivalent circuit of the induction motor including the harmonic machines. The maximum impedance between points B and C Z_{BC} is of the order of 1...2 % of Z_{AC}.

It can be shown that the maximum value of the impedance between points B and C with reference to Fig. 13 Z_{BC} is of the order of 1...2 %, of Z_{AC} and hence calculations are much simplified if Z_{BC} is ignored in calculating the currents in the motor windings. Thus, the motor currents are calculated for various values of slip by considering the fundamental field only. The performance of the harmonic fields can be determined by considering them as constant current phenomena.

Considering the air gap and stator phenomena the magnetizing reactance of the ν:th harmonic referred to the stator is (Agarwal 1960)

$$X_{m\nu} = X_{m1} \cdot \frac{1}{\nu^2} \left(\frac{\xi_\nu}{\xi_1}\right)^2 . \tag{183}$$

This is not quite valid for the stator phenomena but since the pole pitches of the harmonics (Eqn. 178) are very short the effects of stator laminations are not more accurately studied.

If constant permeability and conductance are used Eqns. 9a, 9b and 11a give

$$\nabla^2 \mathbf{H} = j\omega_{\nu r}\sigma\mu \mathbf{H} . \tag{184}$$

Because the pole pitch of the harmonic ν is small, the end effects are ignored and the problem is considered as a plane wave penetrating into a conducting media:

$$\frac{\partial^2 \overline{H}_{x\nu}}{dy^2} - j\omega_{\nu r}\sigma\mu \overline{H}_{x\nu} = 0 . \tag{185}$$

If the co-ordinates are so chosen that $y = 0$ at the surface of the rotor the solution for Eqn. 185 is using constants $\overline{A}_1$ and $\overline{A}_2$

$$\overline{H}_{x\nu} = \overline{A}_1 \, e^{\frac{1+j}{\sqrt{2}} \sqrt{\omega_{\nu r}\sigma\mu}\; y} + \overline{A}_2 \, e^{-\frac{1+j}{\sqrt{2}} \sqrt{\omega_{\nu r}\sigma\mu}\; y} . \tag{186}$$

Because $\overline{H}_{x\nu}$ must vanish when y goes towards minus infinity, $\overline{A}_2$ must be zero. The solution is

$$\overline{H}_{x\nu} = \overline{H}_{0x\nu} \, e^{\frac{1+j}{\sqrt{2}} \sqrt{\omega_{\nu r}\sigma\mu}\; y} . \tag{187}$$

The axial electric field strength is

$$\overline{E}_{z\nu} = \frac{1}{\sigma} \frac{\partial}{\partial y} \overline{H}_{x\nu} = \frac{1}{\sigma} \frac{1+j}{\sqrt{2}} \sqrt{\omega_{\nu r}\sigma\mu}\; \overline{H}_{x\nu} . \tag{188}$$

The relation between the electric and magnetic field strengths is called the surface impedance of the harmonic ν:

$$\overline{Z}_{\nu} = \frac{\overline{E}_{zy}{}^{\swarrow\,\nu}}{\overline{H}_{x\nu}} = \frac{1 + j}{\sigma\sqrt{2}}\sqrt{\omega_{\nu r}\sigma\mu}\,. \tag{189}$$

A similar equation to Eqn. 146 can be written for the harmonic ν

$$\overline{\theta}_{\nu} = \frac{4}{\pi}\,\frac{m}{2}\,\frac{\xi_{\nu}N}{p_{\nu}}\,\sqrt{2}\;\overline{I}'_{r\nu} = \int_{-\tau_{\nu}}^{0} \overline{H}_{rx\nu}\,e^{ja_{\nu}x}\,dx = \frac{2\overline{H}_{rx\nu}}{j\,a_{\nu}}\,, \tag{190}$$

$$\overline{I}'_{r\nu} = \frac{H_{rx\,\nu}\;p\nu\,\pi}{m\,\xi_{\nu}\;N\;\sqrt{2}\;\;j\,a_{\nu}}\,, \tag{191}$$

where $a_{\nu} = \frac{\pi}{\tau_{\nu}} = \frac{2\,p\nu}{D}$. The harmonic ν induces a voltage, which is referred to stator:

$$\overline{U}'_{r\nu} = -j\omega_s\frac{N\xi_{\nu}}{\sqrt{2}}\int_{-\frac{\tau_{\nu}}{2}}^{\frac{\tau_{\nu}}{2}} \overline{B}_{ry\nu}\,e^{ja_{\nu}x}L\,dx = -\,j\,\frac{2\omega_s N\,\xi_{\nu}\;L}{\sqrt{2}\;\;a_{\nu}}\,\overline{B}_{ry\nu}\,. \tag{192}$$

The normal flux density $\overline{B}_{ry\nu}$ can be expressed by the axial electric field strength $\overline{E}_{rz\nu}$:

$$\overline{E}_{rz\nu} = -\,\frac{\omega_{r\nu}}{a_{\nu}}\,B_{ry\nu}\,. \tag{193}$$

The rotor harmonic impedance is now written:

$$\overline{Z}'_{r\nu} = \frac{\overline{U}'_{r\nu}}{\overline{I}'_{r\nu}} = \frac{2\;\omega_s}{\omega_{r\nu}}\,(N\,\xi_{\nu})^{2}\,\frac{mL}{p\,\tau_p}\,\frac{\overline{E}_{rz\nu}}{\overline{H}_{rx\nu}}\,. \tag{194}$$

The surface impedance of the ν:th harmonic in Eqn. 189 may now be referred to the stator with the help of Eqn. 194.

7.2 Slot harmonics

In machines which posses open or semiclosed stator slots the induction on the surface of the rotor is modulated in a cumbersome way by the alternations of the air gap permeance. In this case where the rotor surface is smooth the problem becomes easier to handle. The stator permeance is assumed to be infinite.

7.2.1 Analysis of the air gap induction alternations

Because the pole pitch τ_p of the fundamental is multiple compared with the tooth pitch τ_s of the stator, the induction can be examined in the area of one tooth pitch, Fig. 14.

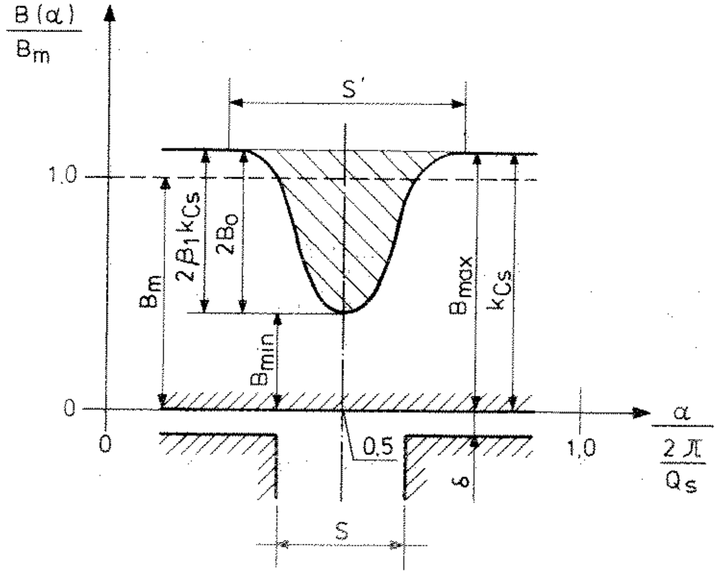

Figure 14. Per unit induction over a stator slot.

The magnetic flux density has a constant value under the teeth and drops under the effective slot width s'. Heller and Hamata (1977) have introduced an equivalent relation for the magnetic induction over the slot pitch. If origin is fixed with the middle point of a tooth this relation is written over one slot pitch with reference to Fig. 14:

$$B(\alpha) = B_{max}\left[\ 1 - \beta_1 - \beta_1 \cos\left(\frac{\pi D}{1.6\,s}\left(\alpha - \frac{2\pi}{2Q_s}\right)\right)\right]$$

for the interval $(\pi/Q_s - 1.6\ s/D) \leq \alpha \leq (\pi/Q_s + 1.6\ s/D)$,

(195)

$$B(\alpha) = B_{max}$$

for the interval $0 < \alpha < (\pi/Q_s - 1.6\ s/D)$, $(\pi/Q_s + 1.6\ s/D) < \alpha < 2\pi/Q_s$

The distribution calculated by the Heller-Hamata-relation is in good agreement with the actual one. Bermann (1982) introduced a Fourier-series to evaluate the induction over one slot pitch τ_s. With reference to Fig. 14 this Fourier-series is written:

$$B(\alpha) = B_m\left[1 - \sum_{k=1}^{\infty} (-1)^k \beta_1 k_{Cs} a_{1k} \cos(k\,Q_s\alpha)\right] \tag{196}$$

where $$a_{1k} = \frac{2\ \sin\left(k\pi\,\frac{s'}{\tau_s}\right)}{k\pi\left[\ 1 - \left(k\,\frac{s'}{\tau_s}\right)^2\right]}\ , \tag{197}$$

$$\beta_1 = \frac{B_0}{B_{max}} = \frac{B_{max} - B_{min}}{2\ B_{max}} = \frac{1 + u^2 - 2u}{2(1 + u^2)}\ ,$$

$$u = \frac{s}{2\delta} + \sqrt{1 + \left(\frac{s}{2\delta}\right)^2}\ ;\quad s' = \frac{\gamma\delta}{\beta_1}\ ;\quad \gamma = \frac{(s/\delta)^2}{5 + s/\delta}\ ; \tag{198}$$

$$k_{Cs} = \frac{\tau_{N1}}{\tau_{N1} - \beta\,s'} = \frac{B_{max}}{B_m}\ ;\quad \delta_e = k_{Cs}\cdot\delta\ .$$

Eqns. 198 are given by Richter (1967). The flux densities given by Eqns. 195 and 196 are compared in Fig. 15 over a stator slot starting at the center of the slot. Close agreement between these two relations is seen. Eqn. 196 is used in further presentation.

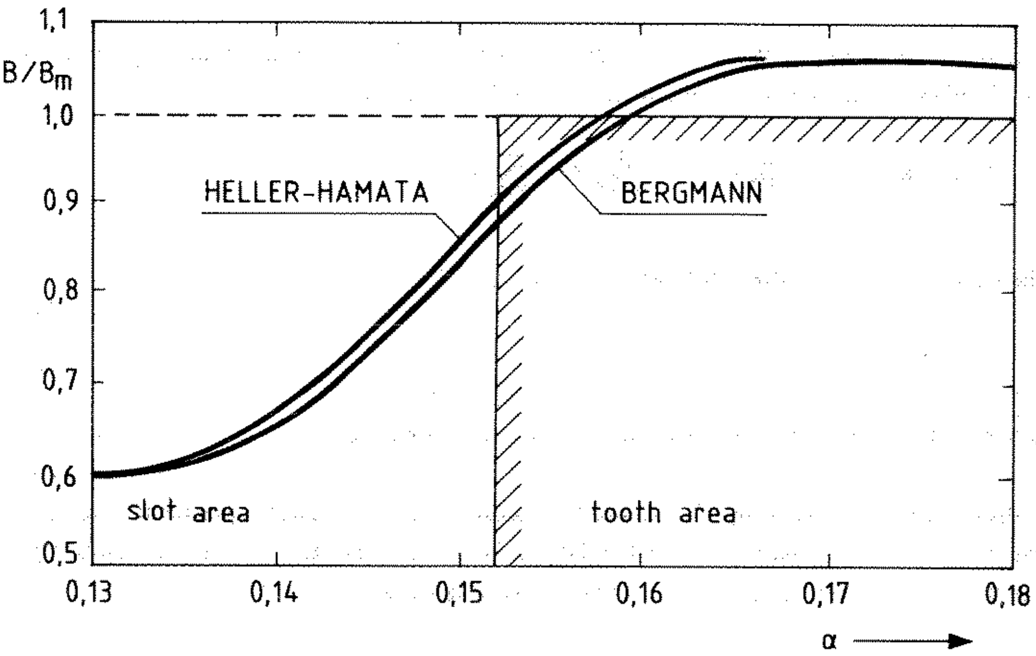

Figure 15. Comparison of the flux densities over a stator slot (δ/s = 0.75 mm/2.2 mm, D = 100 mm, $Q_s = 24$) given by Eqns. 195 and 196.

The sentence in brackets in Eqn. 196 represents the permeance function of the slotted air gap. Since factor a_{1k} decreases quite rapidly it is possible to describe the fluctuation in B(α) by the first five terms of the Fourier-series.

If we consider an arbitrary magnetomotive force which is superposed on the permeance function of the slotted air gap, we must find out how these work together. The angle α is measured starting in the middle of the coil section of phase U, Fig. 16.

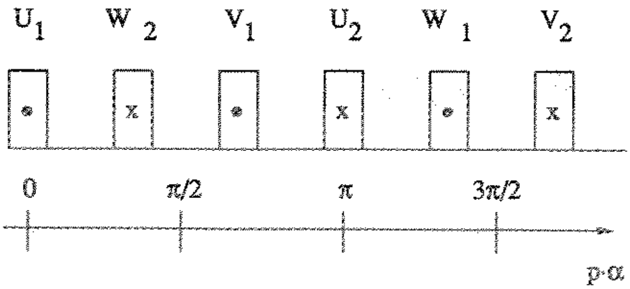

Figure 16. The co-ordinate system to calculate the slot harmonics.

Using Eqn. 190 to calculate the individual harmonic mmfs the resulting air gap magnetomotive force in a three phase machine ($m = 3$) is

$$\bar{\theta}_0(\alpha) = \sum_{\substack{\nu=6g+1 \\ g=-\infty}}^{+\infty} j\,\bar{\theta}_{0\nu}\, e^{-j\nu\alpha}\,, \tag{199}$$

The following annotation will be used:

$$\sum_{\nu} = \sum_{\substack{\nu=6g+1 \\ g=-\infty}}^{+\infty}\,. \tag{200}$$

The place dependent permeance function corresponds to the inverse of the air gap

$$\frac{1}{\delta(\alpha)} = \frac{1}{\delta_e}\left[\, 1 - \sum_{k} b_{1k}\left(e^{\,j kQ_s\alpha} + e^{-j kQ_s\alpha}\right) \right] \tag{201}$$

$$b_{1k} = \frac{1}{2}\,\beta_1\, k_{Cs}\, a_{1k}\left((-1)^k\right)^{q_s + i_{N1} + 1}\,. \tag{202}$$

Factor $((-1)^k)^{q_s + i_{N1} + 1}$ takes into consideration the position of a tooth or slot depending on the number q_s of stator slots per phase and pole and the number i_{N1} by which the coil span deviates from the pole pitch. Since

$$\frac{Q_s}{p} = 2\, m_s q_s = 6\, q_s\,,$$

the air gap induction can be written as

$$B(\alpha) = j\,\frac{\mu_0}{2\delta_e}\sum_{\nu}\;\bar{\theta}_{0\nu}\left[\, e^{-j\nu p\alpha} - b_{1k}\left(e^{-j(\nu+6kq_s)p\alpha} + e^{-j(\nu-6kq_s)p\alpha}\right) \right]. \tag{203}$$

Here the windings induced magnetomotive forces have been multiplied by the inverse of the air gap function for an individual value of k which gives place dependent induction $B(\alpha)$. Although the air gap is not smooth and thus additional harmonics exist, the ordinals of all harmonics still follow pattern $\nu = 6g+1$. This gives an opportunity to rewrite Eqn. 203 in the form

$$B(\alpha) = j\frac{\mu_0}{2\delta_e}\sum_{\nu}\left[\ \bar{\theta}_{0\nu} - b_{1k}\left(\bar{\theta}_{0(\nu+6kq_s)} + \bar{\theta}_{0(\nu-6kq_s)}\right)\right] e^{-j\nu p\alpha}\,. \tag{204}$$

Eqn. 204 gives the opportunity to calculate the stator induced voltage:

$$\bar{U}_{s\delta} = \sum_{\nu}\ jX_{sm\nu}\left[\ \bar{I}_{0\nu} - b_{1k}\frac{\xi_{s(\nu+6kq_s)}}{\xi_{s\nu}}\ \frac{\nu}{\nu+6kq_s}\ \bar{I}_{0\,(\nu+6kq_s)}\right.$$

$$\left. + \frac{\xi_{s(\nu\ -\ 6kq_s)}}{\xi_{s\nu}}\ \frac{\nu}{\nu-6kq_s}\ \bar{I}_{0\,(\nu-6kq_s)}\right]\ . \tag{205}$$

Here $X_{sm\nu}$ is the magnetizing reactance of the ν:th harmonic motor (Eqn. 183). The annotation

$$b_{1k} = \frac{\xi_{s(\nu\,\pm\,6\,kq_s)}}{\xi_{s\nu}} = \frac{1}{2}\,\beta_1\,k_{Cs}\,a_{1k}\,, \tag{206}$$

which is obtained using Eqn. 202 and the definition of the winding factor, simplifies Eqn. 205:

$$\bar{U}_{s\delta} = \sum_{\nu}\ jX_{sm\nu}\left(\bar{I}_{0\nu} - \bar{I}_{0\nu k+} - \bar{I}_{o\nu k-}\right) \tag{207}$$

$$\bar{I}_{0\nu k\pm} = \frac{1}{2}\,\beta_1\,k_{Cs}\,a_{1k}\frac{\nu}{\nu\pm 6\,kq_s}\ \bar{I}_{0\,(\nu\pm 6\,kq_s)}\,. \tag{208}$$

Eqns. 207 and 208 are valid for all kinds of three phase single- and two-layer windings. According to Eqn. 207 the ν:th harmonic motor can be illustrated as in Fig. 17. The source currents of Fig. 17 are determined by Eqn. 208 which shows that the fundamental motor and the harmonic motors cannot be solved separately because they have an effect on each other via the current sources. Harmonic machines, the ordinal of which deviate by $\pm 6kq_s$, create the current sources of the harmonic motor ν. An iterative solution is thus unavoidable. Bergmann (1982) has shown that the power related with the current sources disappears since every source power has a counterpart that makes the power sum zero. Thus the current sources do not disturb the power balance of the machine.

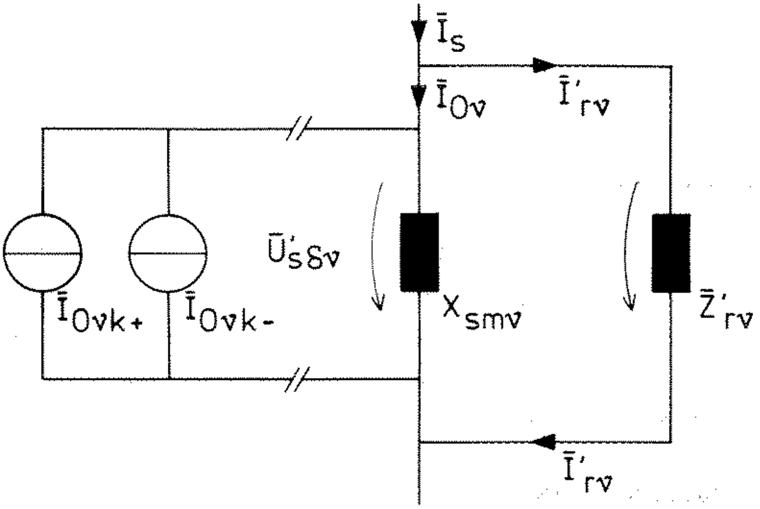

Figure 17. Equivalent circuit for the ν:th harmonic motor. The numerous current sources represent the effect of stator slots and they generate additional voltages in the magnetizing reactance.

This method, however, is quite cumbersome because every harmonic machine is connected with numerous other machines via the permeance function. Big mistake is not made if the method is simplified by leaving out all slot waves that are generated without the fundamental. This can be done because the winding factors of anything other than the slot harmonics are small. Slot harmonics do occur at ordinals

$$\nu = k\frac{Q_s}{p} + 1 \text{ , } k = \pm 1 \pm 2 \pm 3 \text{ ...,} \tag{208}$$

and they have the same winding factor as the fundamental. Examining Eqns. 207 and 208 shows that at ordinals $\nu < (6\ k\ q_s)$ the winding harmonics and the slot harmonics strengthen each other since a $_{1|k|}$ is positive and otherwise weaken each other. If the method is simplified the voltages of the slot harmonics are

$$\bar{U}_{s\delta(1+6kq_s)} = j\,X_{sm(1+6kq_s)}\left[\ \bar{I}_{0(1+6kq_s)} - \frac{1}{2}\,\beta_1\,k_{Cs}\,a_{1|k|}\,(1+6kq_s)\,\bar{I}_{01}\right]$$

$$k = \pm 1, \pm 2, \pm 3 \text{...} \tag{209}$$

8. RESULTS

8.1 Test motor and test arrangement

The theory of the previous chapters is applied to the calculation of the operation characteristics of different smooth massive rotors of a 12 kW 400 Hz induction machine. The motor has a conventional three-phase stator with semiclosed slots. The main parameters of the test motor are given in Table 2.

Table 2. Parameters of the solid rotor test motor.

Number of pole pairs, p	1
Number of phases, m	3
Number of stator slots, Q_s	24
Number of stator slots per phase and pole, q_s	4
Number of turns in series per phase of stator winding, N	14
Winding factor, ξ	0.9577
Stator outer diameter/mm	235
Stator bore/mm	100
Width of the stator slot opening/mm	2.2
Stator length/mm	100
Stator stack length/mm	96
Stator cooling channel width/mm	4
Air gap, δ/mm	0.75
Rotor diameter D/mm	98.5
Rotor length*/mm	100
Rated voltage U_s/V	225/130
Connection	star
Rated current, I_s/A	65
Rated frequency f/Hz	400
Stator resistance, R_s/mΩ at 20 C, 400 Hz	26
Stator leakage inductance, $L_{s\sigma}$ /μH	68.4
* in the calculations the rotor and the stator were assumed to be of equal length, L = 96 mm, and thus the effect of stator cooling channel was neglected	

The winding scheme of the stator and the form of the stator slots are given in Fig. 18.

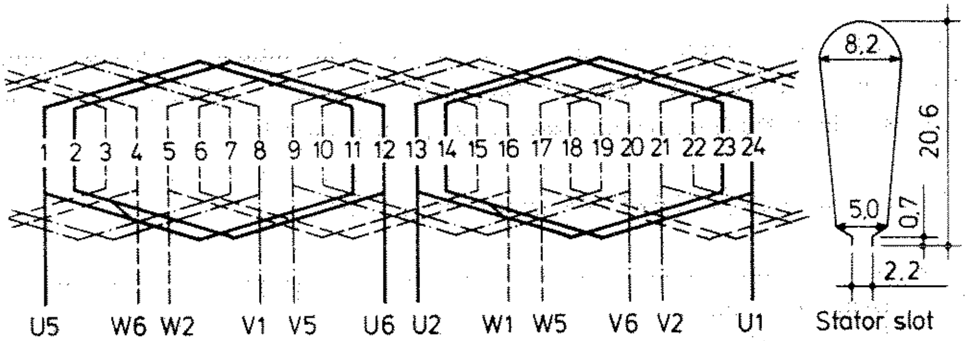

Figure 18. The winding scheme of the stator and the form of the stator slot; The winding is made of round enameled copper wire. There are 98 wires per slot, 14 wires in parallel of which 5 are 0.8 mm in diameter and 9 0.85 mm in diameter. Points U_1- U_5 and U_2- U_6 are connected together to form two branches in parallel. Analogous connections are made in other phases, too. The total weight of stator copper is 5 kg. Material of the stator laminations: Surahammars Bruk. CK-30

The high speed motor was tested with the measurement system presented in Fig. 19.

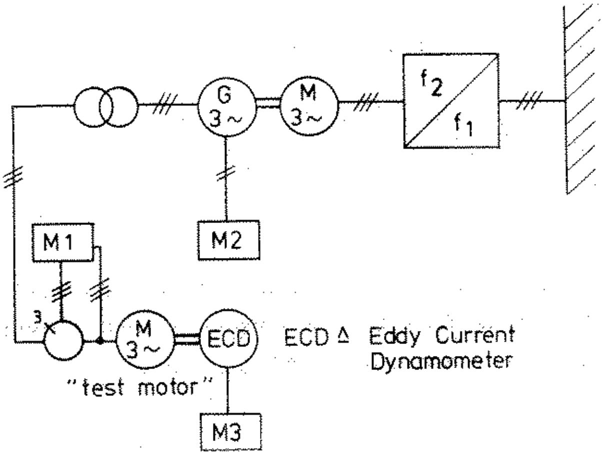

Figure 19. The test arrangement of the 12 kW 400 Hz induction motor. Strömberg SAMI 100 F inverter supplies a 170 kW two-pole induction motor which turns a 70 kVA nine-pole brushless synchronous generator. The test motor is loaded by a water cooled eddy current dynamometer 2 WB 65 HS manufactured by Vibro Meter. The supply frequency of the test motor can be controlled between 150 Hz and 550 Hz and the voltage between 0 V and 440 V. The eddy current dynamometer contains a PID-controller to adjust the speed of the test motor by controlling the load torque. The measuring devices are: M1, Norma AC-POWER Analyzer D 5155 with three Norma current transformers (voltage, current, power factor, power; inaccuracy smaller than ±0,5 % of range); M2, Philips PM 6670 counter (frequency; inaccuracy smaller than 10^{-6} Hz); M3, Vibro Meter electronics 234-213-000 (torque, speed, power; inaccuracy smaller than ±0,5 % for torque and smaller than 1 digit for speed).

8.2 Rotor materials

Six rotors made of different materials were tested. The materials included three construction steels, pure iron, an aluminium alloy and a mixture of cobalt and iron. The chemical consistencies of the ferromagnetic materials are given in Table 3.

Table 3. Chemical consistencies of the ferromagnetic rotor materials.

Table 3.	additive% at least % at most									
MATERIAL	C	Si	Mn	P	S	Cr	Ni	Mo	V~~n~~	Co
Vacofer S1*	-	-	-	-	-	-	-	-	-	-
(Pure Iron)	0.007	-	-	-	0.0015	0.01	0.006	0.006	-	-
Vacoflux 50*	-	-	-	-	-	-	-	-	-	-
(FeCo)	0.007	-	-	-	0.0015	0.01	0.006	0.006	2.0	49,0
MoC 315M**	0.32	0.15	0.50	-	-	1.20	12.0	0.15	-	-
(steel)	0.39	0.40	0.80	0.035	0.035	1.60	1.60	0.25	-	-
Fe 520	-	0.15	0.90	-	-	-	-	-	-	-
(steel)	0.18	0.55	1.50	0.040	0.045	-	-	-	0.09	-
Fe 52	-	-	-	-	-	-	-	-	-	-
(steel)	0.20	0.55	1.50	0.045	0.045	-	-	-	-	-

* Trade marks of Vacuumschmeltze GmBH

** Trade mark of Ovako Steel

The magnetic properties of the different rotor materials were measured on rings and the resistivities ρ and the temperature coefficients ε of resistivities were measured on broken rings with 1 A/mm² direct current density and are given in Fig. 20a, b, c, d, e.

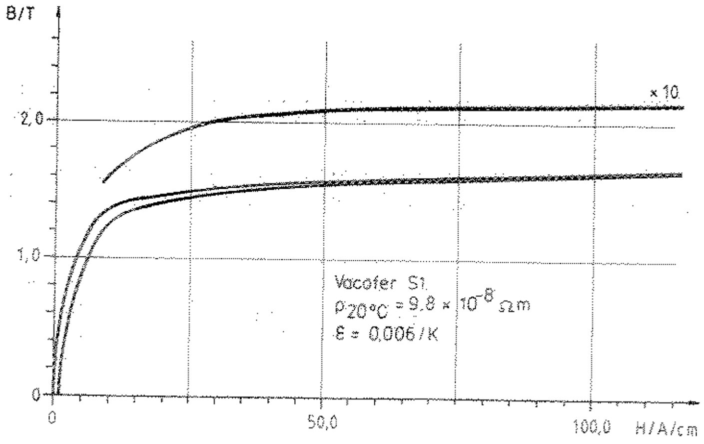

(a)

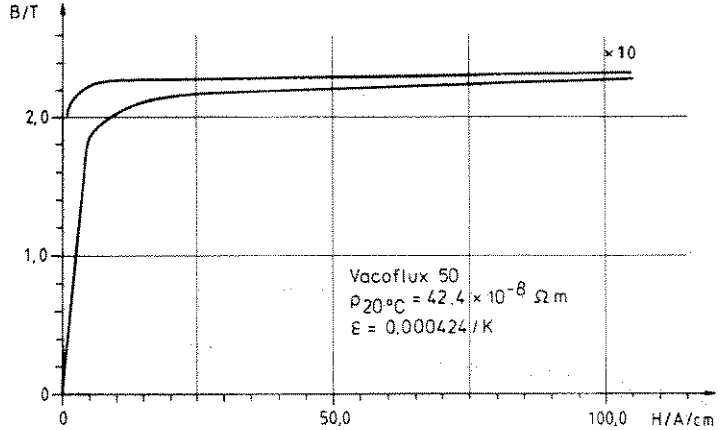
B/T
2,0
1,0
0
0
50,0
100,0
H/A/cm
×10
Vacoflux 50
$\rho_{20°C} = 42{,}4 \times 10^{-8}\ \Omega m$
$\varepsilon = 0{,}000424/K$

(b)

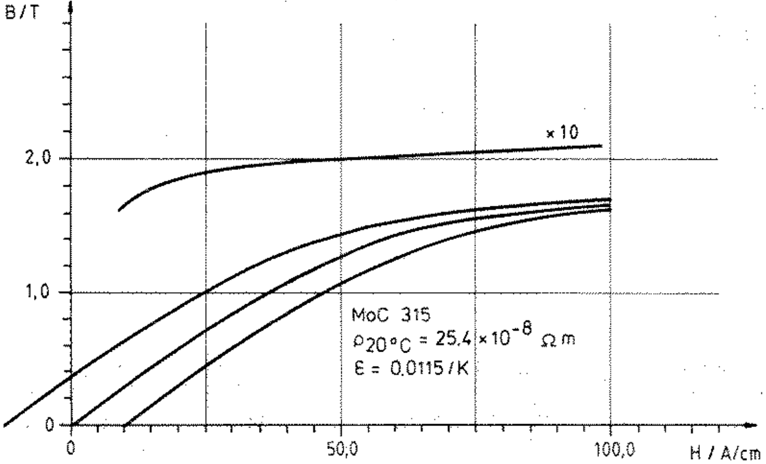
B/T
2,0
1,0
0
0
50,0
100,0
H / A/cm
×10
MoC 315
$\rho_{20°C} = 25{,}4 \times 10^{-8}\ \Omega m$
$\varepsilon = 0{,}0115/K$

(c)

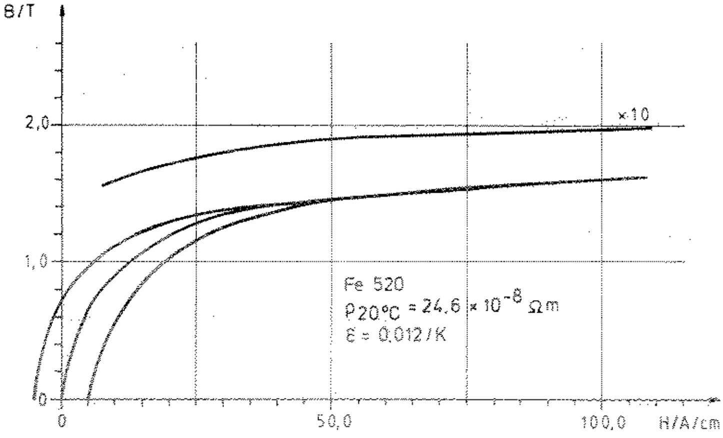
B/T
2,0
1,0
0
0
50,0
100,0
H/A/cm
×10
Fe 520
$\rho_{20°C} = 24{,}6 \times 10^{-8}\ \Omega m$
$\varepsilon = 0{,}012/K$

(d)

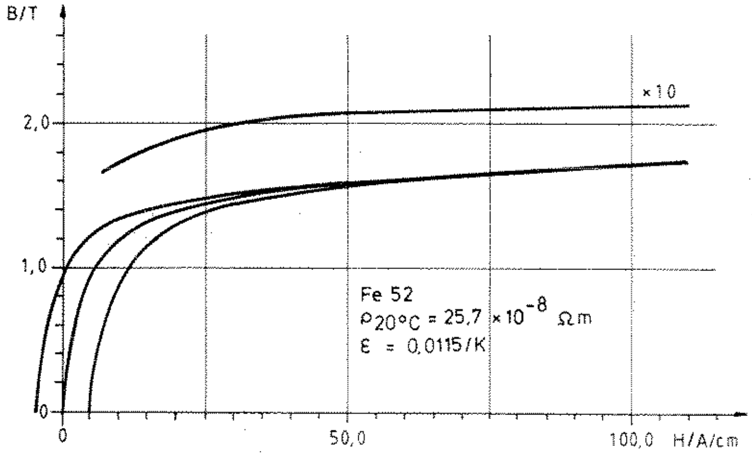

(e)

Figure 20. Electromagnetic properties of the ferromagnetic rotor materials (a) Vacofer S1, (b) Vacoflux 50, (c) MoC 315M, (d) Fe520, (e) Fe52. The B-H-hysteresis loops were measured on rings with direct current magnetization. The average curves were used in calculations. The resistivities ρ and the temperature coefficients ε of the resistivities were measured on broken rings with 1 A/mm² direct current density.

The aluminium alloy tested was Al Si 1 Mg the resistivity of which is $\rho_{20^oC} = 3{,}8 \cdot 10^{-8}$ and the temperature coefficient $\varepsilon = 4{,}0 \cdot 10^{-3}\ K^{-1}$. The permeability of the alloy is approximately the same as the permeability of free space.

8.3 No-load characteristics of different rotors

The motor was driven with a synchronous generator at 400 Hz supply frequency. The No-load test with Fe520-rotor was performed using three rotor diameters 98.5 mm, 98.0 mm and 97.5 mm and consequently three air gaps δ (0.75 mm, 1 mm and 1.25 mm respectively) to check the validity of the method for calculating the stator harmonics. The results of these measurements are given in Fig. 21.

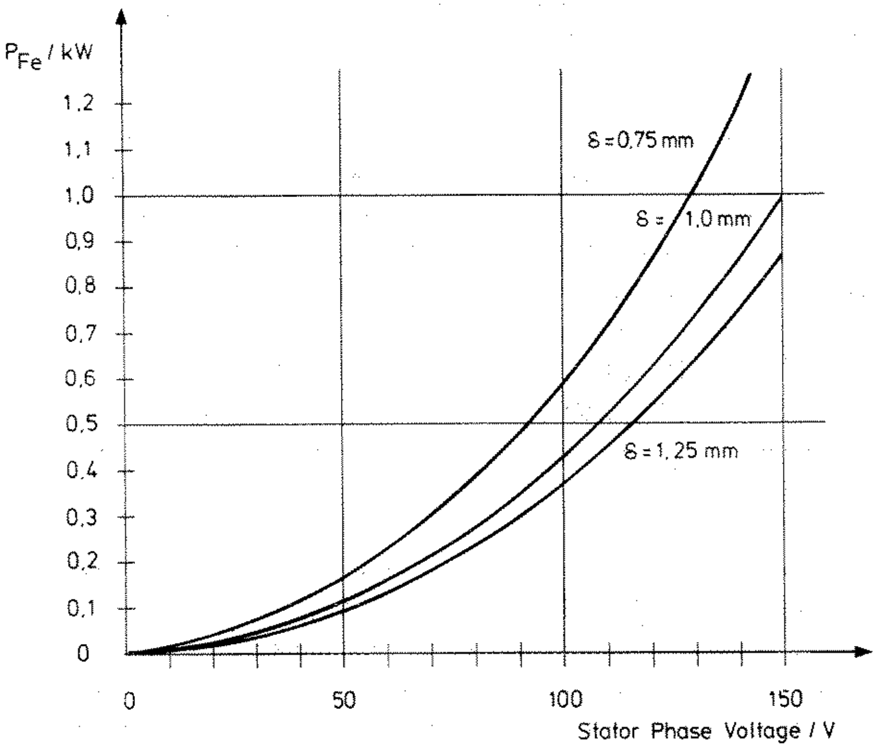

Figure 21. Measured no-load losses with three Fe520-rotors of different diameters friction losses and stator copper losses subtracted, supply frequency 400 Hz.

The stator currents were 21.1 A, 26.0 A and 30.5 A at 130 V respectively. The stator core loss at 130 V 400 Hz was evaluated with conventional methods to be about 200 W. When this value was subtracted from the values of the curves of Fig. 20 the no-load losses of the rotors were found. The rotor loss decreases from 800 W via 550 W to 450 W at the nominal phase voltage of 130 V when the air gap increases from 0.75 mm to 1.25 mm. Using the incremental permeability $\mu_r = 40\ \mu_0$ that Bergmann (1982) suggests gives astonishingly good calculation results at this no-load operation point. The calculated rotor losses were 809 W, 570 W and 448 W respectively.

There were some difficulties in obtaining the different materials and this was the reason for the fact that in all rotors the nominal rotor diameter of 98.5 mm was not reached. Table 4 gives the different rotor diameters and no-load losses at U_{ph} = 130 V, 400 Hz nominal point.

Table 4. Measured no-load losses with different rotors. The values in parenthesis are calculated to correspond to 0.75 mm air gap.

Material	Rotor diam./δ/mm	I/A	Rotor loss/kW at 130 V, 400 Hz
Vacofer S1	98.30/0.85	24.1	0.80 (0.86)
Vacoflux 50	98.50/0.75	20.7	0.71
Mo C 315 M	98.50/0.75	21.1	0.81
Fe 520	98.50/0.75	21.1	0.80
Fe 52	98.15/0.925	25.5	0.68 (0.81)

According to calculations the loss of Vacofer S1 would increase to 860 W if the air gap were 0.75 mm and the loss of Fe52 would increase to 810 W in the same case (in parenthesis in Table 4). These losses are mainly caused by the slot harmonics of the stator. The higher the resistivity of the rotor material is the lower is the loss caused by the slot harmonics.

The aluminium alloy rotor was also tested and it became quite obvious that aluminium cannot be used as rotor material with this kind of stator. The No-load running speed of the aluminium rotor was 600 rpm at 45 V, 200 A, 400 Hz. The starting torque of the rotor was about 0.5 Nm at 45 V, 200 A, 400 Hz. These figures show that fundamental magnetic flux penetrates weakly into the aluminium rotor when using normal stator construction and the leakage fluxes of the machine mainly determine its behaviour.

8.4 Loaded running motor

The most interesting working area of the high speed induction motor is at small slip. The motor equipped with different rotors was loaded by a high speed eddy current dynamometer which was equipped with a speed control unit to predetermine the slip. This made it possible to trace the torque vs. speed characteristics of the different rotors. These measured characteristics are given in Fig. 22.

The figure clearly indicates the large differences at low slip. The highest torque is reached with Vacofer S1 which has the lowest resistivity of the ferromagnetic materials tested and 2.15 T saturation flux density. The extremely high saturation flux density 2.3 T

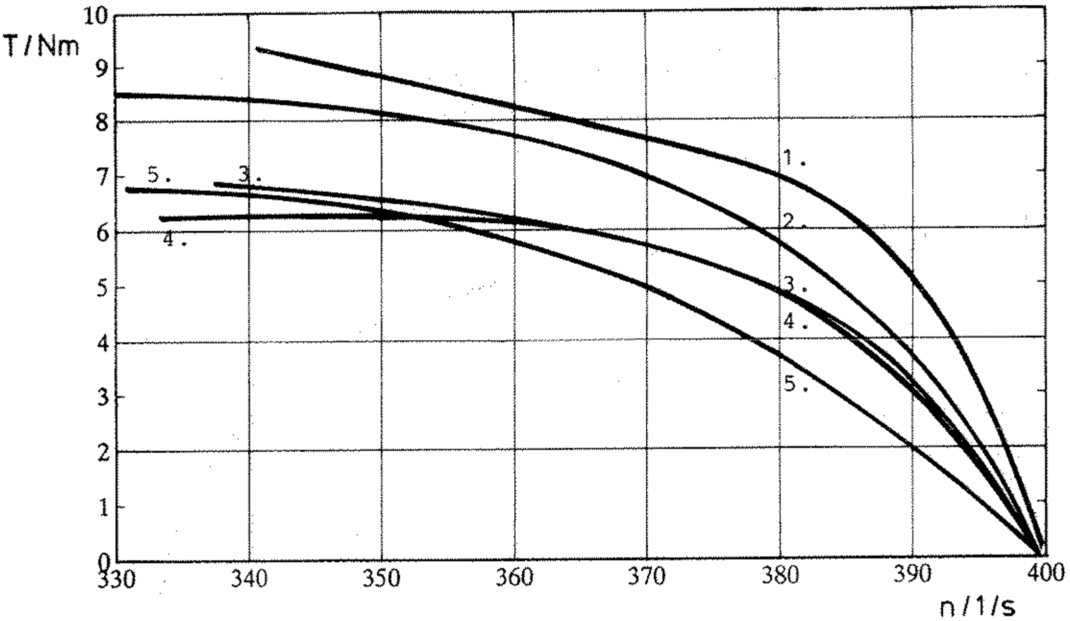

Figure 22. The measured torque of the test motor equipped with different rotors as a function of the rotational speed, at nominal voltage, U_{ph} = 130 V, 400 Hz. The curves are: 1. Vacofer S1, 2. Fe 52, 3. Fe 520, 4. MoC 315, 5. Vacoflux 50

of Vacoflux 50 is not enough to make it a good material because of its quadruple resistivity compared with Vacofer S1. At a slip of 10 Hz 12.8 kW output power was measured for Vacofer S1 and 9.3 kW for Fe 52 while only 4.8 kW was reached with Vacoflux 50. So Vacofer gives 38 % higher and 167 % higher torque at 10 Hz slip than Fe 52 and Vacoflux 50 respectively. The difference between Fe 52, Fe 520 and MoC 315 gives an indication of the effect of the permeability of the rotor material since the resistivities of these three materials are almost the same but large differences are measured between the B-H-curves.

The flexible disc pack coupling between the motor and the dynamometer generated a 500 W friction loss at 400 Hz rotating frequency. So the total friction loss of the assembly at nominal speed varied between 600 W and 750 W depending on the rotor diameter. This has been taken into account when comparing the calculated electromagnetic torque of the machine with the measured values. In the following figures the calculated and measured torque, current and power factor versus rotating speed are presented for Vacofer S1 and Fe52 which gave the highest torques at low slip. . During the measurements the temperature of the stator windings was kept under 150 °C. The highest rotor temperature measured after rapid stop was about 250 °C. The rotor temperature creates a quite large possibility of error since rotor resistivity is a very significant factor when calculating the performance of the motor. In the computations, constant temperatures of 140 °C and 200 °C were used for stator and rotor respectively.

The torque, current, power factor and efficiency of Vacofer S1 and Fe52-rotors as functions of the rotating speed are shown in the following figures.

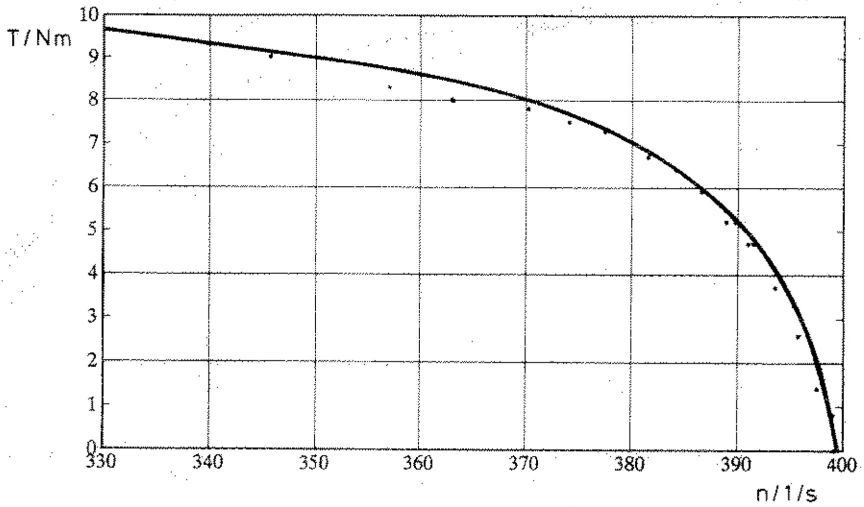

Figure 23. The torque T computed and measured for the test motor equipped with Vacofer S1-rotor as a function of the rotational speed, U_{ph} = 130 V, 400 Hz. (Computation, solid line; Measurement, dots)

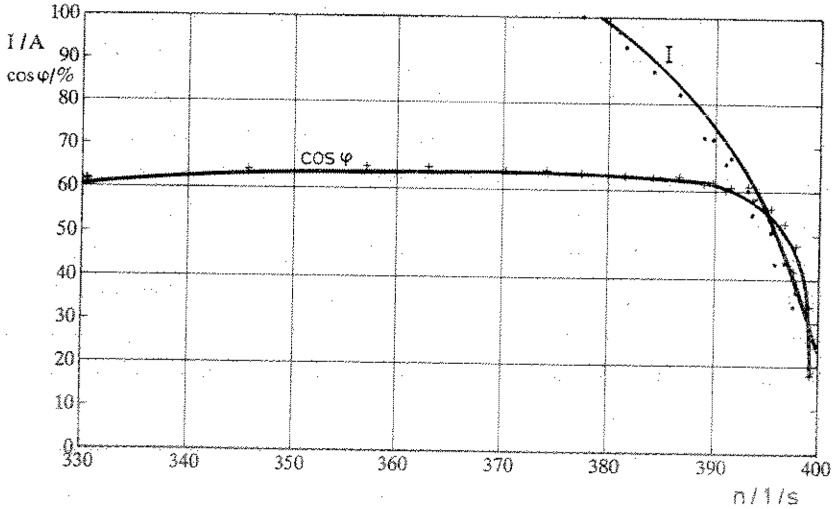

Figure 24. The current I and power factor cosφ computed and measured for the test motor equipped with Vacofer S1-rotor as a function of the rotational speed, U_{ph} = 130 V, 400 Hz. (Computation, solid line; Measurement, dots for current, + for cosφ).

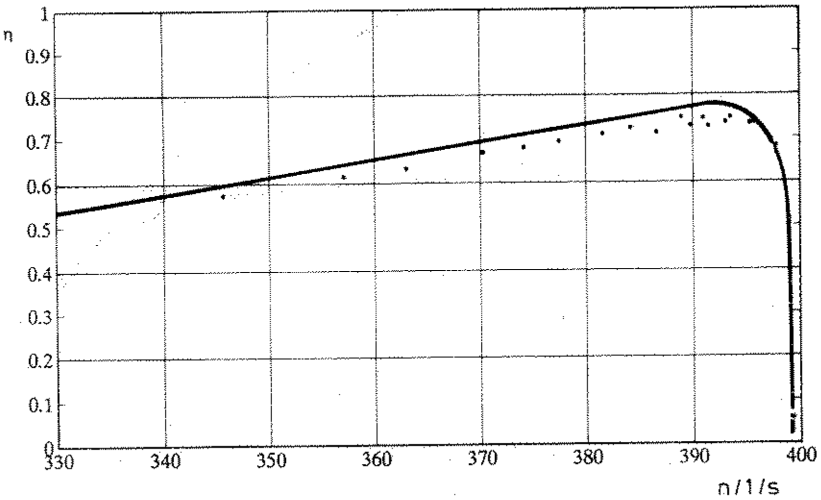

Figure 25. The efficiency η computed and measured for the test motor equipped with Vacofer S1-rotor as a function of the rotational speed, U_{ph} = 130 V, 400 Hz. (Computation, solid line; Measurement, dots).

When calculating the effects of harmonics in this rotor the value $\mu_r = 40\ \mu_0$ that Bergmann-(1982) suggested for the incremental permeability seemed not to give good agreement with the measured values. Value $\mu_r = 80\ \mu_0$ was used instead. The permeability to calculate the flux Φ_2 (Fig. 6) was chosen from the B-H-curve at the point of 1.5 T.

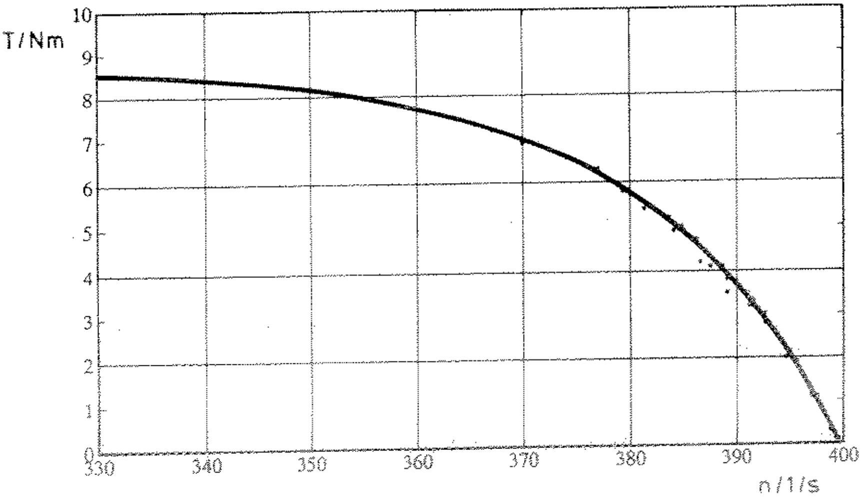

Figure 26. The torque T computed and measured for the test motor equipped with Fe52-rotor as a function of the rotational speed, U_{ph} = 130 V, 400 Hz. (Computation, solid line; Measurement, dots)

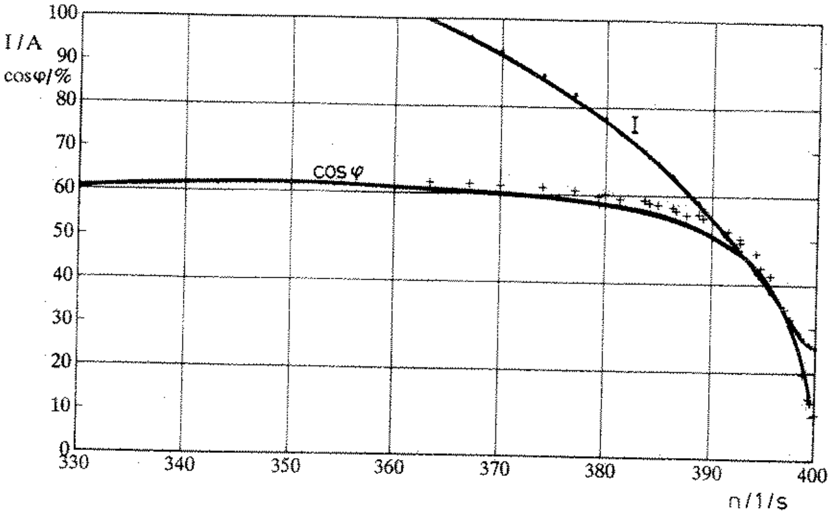

Figure 27. The current I and power factor cosφ computed and measured for the test - motor equipped with Fe52-rotor as a function of the rotational speed, U_{ph} = 130 V, 400 Hz. (Computation, solid line; Measurement, dots for current, + for cosφ)

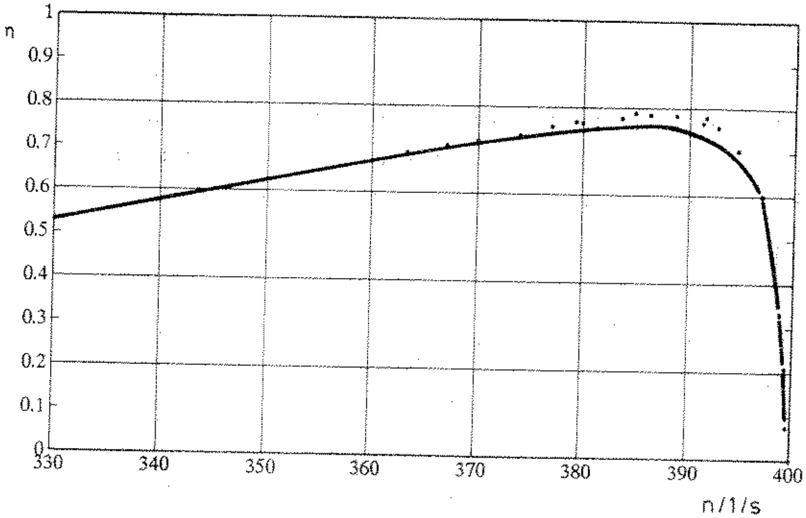

Figure 28. The efficiency η computed and measured for the test motor equipped with Fe52-rotor as a function of the rotational speed, U_{ph} = 130 V, 400 Hz. (Computation, solid line; Measurement, dots)

Value $\mu_r = 40\ \mu_0$ for the incremental permeability seemed to be quite valid for calculating the effect of harmonics in the Fe52-rotor in the working area. The permeability to calculate the flux Φ_2 (Fig. 6) was now also chosen from the B-H-curve at the point of 1.5

All the rotors were tested in the slip range of 0 to 1. The effects of harmonics created a saddle-torque curve when the supply frequency was 300 Hz or higher. At 200 Hz supply frequency no saddle-torque was measured. Figure 29. shows the torque behaviour of the Fe52-rotor at lowered phase voltage $U_{ph} = 100$ V, 400 Hz. Slip varies between 0 and 1.

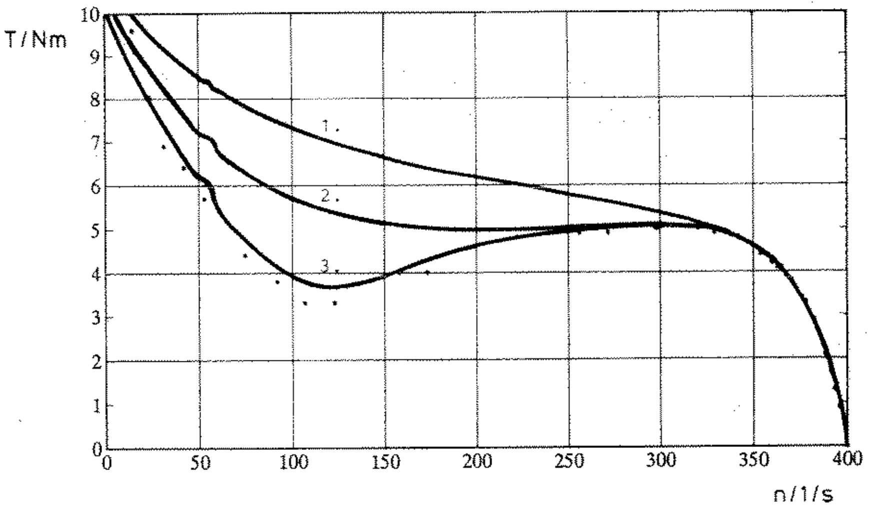

Figure 29. The torque measured and calculated for the test motor equipped with Fe52-rotor as a function of the rotational speed at lowered voltage, $U_{ph} = 100$ V, 400 Hz. Curves 1, 2 and 3 are computed using different values for the incremental permeability, see text. (Computation, solid line; Measurement, dots).

Lowered voltage was used to reduce extremely high rotor losses and thus make the measurement somewhat easier. In addition to the measured points there are three computed curves. The first curve was calculated assuming constant incremental permeability $\mu_r = 40\ \mu_0$ when computing the effect of harmonics in the slip range of 0.2 to 0.95. It is seen that this incremental permeability does not give high enough negative torque for the harmonics. This is an indication of the fact that the rotor saturation with respect to the harmonics changes, when the fundamental saturation changes. The second curve was computed using the incremental permeability $\mu_r = 40\ \mu_0$ in the slip range of 0 to 0.2 and one fourth of the fundamental permeability at the rotor surface at higher slip when this value was under $40\ \mu_0$. The third curve was computed with the same method but using one-tenth of the fundamental permeability μ_1 computed by the multi-layer transfer-matrix method on the rotor surface. This gave the value of about $\mu_r = 10\ \mu_0$ for the incremental permeability in the slip range of 0.6 to 1.0. This indicates that the effect of harmonics at high slip should be more accurately calculated so that the permeability concerning different harmonic waves could be determined during the computing process. The prerequisite for the method presented here is that the permeability of the harmonics is known in advance. Accurate knowledge of the permeability concerning different harmonics is very difficult to obtain. In addition to the fundamental, forty harmonics from -119 to +121 were taken into account during the computation.

Figure 30 gives some indication of the depth of penetration of the fundamental magnetic field density wave in solid rotor material. It also shows how the amplitude of the fundamental magnetic field density increases with slip. The surface of the rotor material is highly saturated and it is possible with reference to the work of Chalmers et.al. (1980) that the value $\mu_r = 10\ \mu_0$ for the incremental permeability is reached in heavily saturated rotor surfaces.

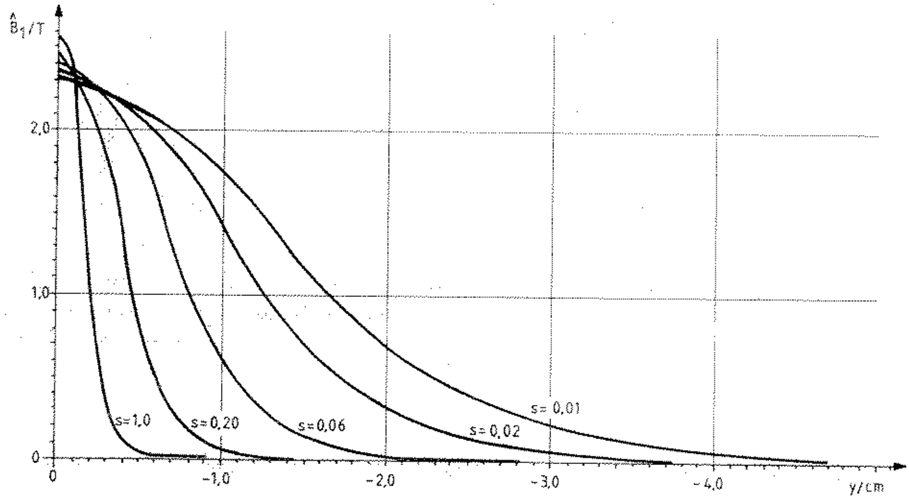

Figure 30. The penetration of the fundamental field density wave into solid rotor material (MoC 315M) with different slips using the multi-layer transfer-matrix method to compute the rotor phenomena with constant current 90 A, 400 Hz in the stator windings.

8.5 Discussion about the results

Since the solution for the electromagnetic fields in the smooth solid rotor of finite length is analytical as far as possible, the computing times are short. The accuracy of the method is fairly good but it necessitates knowledge of some parameters beforehand. This makes the application of the method difficult at large slip if no test results are available. The main working slip area can be fairly reliably calculated. The end effects have significant influence on the rotor behaviour. The greater the slip the greater are the end effects.

The most significant factor that complicates the comparison between the measured and computed results is the temperature of the machine. The high currents in torque versus speed measurements cause elevated resistive losses which rapidly raise the temperature of the rotor. In high speed machines where the rotors are small the temperature rise may be very rapid. The temperature has a remarkable effect on the resistivity of the stator windings and the rotor material and thus on the performance of the machine. As it is difficult to measure the temperature of the rotor during the test, the duration of the test should be as short as possible in order to limit the temperature rise. In addition the machine should have reached a steady state before measuring steady-state quantities.

During the tests the temperature of the stator windings was kept under 150 ^{o}C and each working point was measured during a period of about 6 seconds starting with the rotor rotating at intended speed and rapidly raising the voltage. The speed control unit of the dynamometer kept the speed constant during the measurement. Despite the extreme care taken to record all test data at about the same temperature, there still remained a possibility of significant error. It is possible to have 25 % or even higher difference between torques measured for cold and warm rotors at small slip. At high slip the difference can reach even higher values. These figures give an idea of the amount of uncertainty that is caused by the impossibility of knowing the exact temperature distribution of the machine.

The temperature approximation (140 ^{o}C for stator and 200 ^{o}C for rotor) used for computing seems to give fairly good agreement between calculated and measured properties. At low slip the error is less than 10 %. The possibility of error is largest at about 300 Hz rotor frequency which means a slip of 0.75. In this area the rotor is heavily saturated and good knowledge of the behaviour of the incremental permeability is needed to obtain satisfactory results. This is perhaps the worst defect of this analytical method since it is virtually impossible to have exact knowledge of the permeabilities of all the different harmonics.

The tests indicate that large variations in machine properties do occur when using different materials. The highest torque is reached with a material that has high saturation flux density and good conductivity. Vacofer S1 is this kind of a material but the effect of slot harmonics should be dampened to achieve high efficiency, too. One method of getting better machine properties is to use axial slits on the rotor surface. The method presented here can also be used, after some modifications, for calculating the behaviour of axially slit massive rotors. The effects of slitting the rotor have not been considered during this work in order to make the comparisons between different materials easier. Another method to dampen the effects of slot harmonics on the rotor surface is to use some ferromagnetic material of high resistivity as a thin layer on the rotor surface. The thickness of the layer should be about the same size as the depth of penetration of the lowest harmonics. The effects of coating the rotor have not been examined either.

The test materials used here are all commercially available and no attempts were made to create a new metal alloy that would possess ideal properties for a high speed solid rotor. In the litterature (Wei, Bing-gui 1987) some mentions of the good properties of copper-iron alloys are found, but during this work no such material was availabe and these qualities remain to be tested in further experiments.

The mechanical strengths of the test materials are such that the weakest (pure iron) tolerates about 35000 rpm and the toughest (MoC 315) about 80000 rpm when used as a smooth rotor, the diameter of which is 100 mm.

9. CONCLUSION

The combined calculation method partly employing the three dimensional linear method and partly the multi-layer transfer-matrix method has been adopted to treat smooth solid rotors. The three-dimensional features of the rotor are taken into account using the two dimensional transfer-matrix method slicewise for the saturated parts of the rotor and the three-dimensional linear method for the unsaturated parts. The equivalent circuit resistance and leakage inductance of the stator were measured beforehand.

The main purpose of the work has been to find out the effect of rotor material parameters on the behaviour of the machine. Rotors made of six different materials were tested. The materials included three construction steels, pure iron, an aluminium alloy and a mixture of cobalt and iron. Test results clearly indicate that the highest torque is reached with the material that has both high saturation flux density and good conductivity. Extremely high saturation flux density or very good conductivity alone do not give good torque for the rotor. Tests with cobalt-iron and aluminium gave an indication of this.

This work creates the interesting question of whether it is possible to find a strong material with a B-H-curve like that of pure iron but with remarkably lower resistivity. The efficiency of a high-torque rotor made of this material could be made better by slitting the surface or by coating it with a high resistivity, ferromagnetic material.

The mathematical solution presented here is analytical as far as possible. The main computing effort consists of the transfer-matrix method and consequently the computing times are short. The computed and measured results agree within 10 % at low slip. At higher slip the effect of harmonics becomes dominant and the rotor saturation becomes complicated to handle. Good agreement between computed and measured quantities is reached also at high slip if the incremental permeability concerning harmonics is correctly chosen.

REFERENCES

Agarwal, P.D. 1959. Eddy-current losses in solid and laminated iron. AIEE trans. 78, pp. 169-181.

Agarwal, P.D. 1960. Equivalent Circuits and Performance Calculations of Canned Motors. AIEE trans. pp. 635-642.

Angst, G. 1962. Polyphase induction motor with solid rotor. Effects of saturation and finite length. AIEE trans. pt. 111, pp. 902-909.

Bergmann, D. 1982. Betriebseigenschaften von wärmerohrgekühlten Asynchronmaschinen mit gerillten Massivrotor und Kurzschlusskäfig unter besonderer Berücksichtigung der Stromrichterspeisung Diss. TH - Aachen. 145 S.

Boller, H.W. Jordan, H. 1963. Über die phasenrichtige Addition der nutharmonischen Wicklungsoberfelder und der Nutungsoberfelder bei phasenreinen-Mehrphasenwicklungen. ETZ-A Bd. 84 H7, S. 235-238.

Bondi, H. Mukherji, K.C. 1957. An analysis of tooth ripple phenomena in smooth laminated pole-shoes. Proc. IEE, Vol 104c, pp. 349-356.

Chalmers, B.J. 1962. Asynchronous performance characteristics of turbogenerators. Proc. IEE, Vol 109a, pp. 301-307.

Chalmers, B.J. Hamdi, E.S. 1982. Multi-layer analysis of composite-rotor induction machines. Electric machines and electromechanics, No. 7, pp. 331-338.

Chalmers, B.J. Spooner, E. Abdel-Hamid, R.H. 1980 Parameters of Solid-rotor induction machines with unbalanced supply. Proc. IEE, Vol 127, Pt. B No. 3, pp. 174-182.

Chalmers, B.J. Woolley, I. 1972. General theory of solid-rotor induction machines. Proc. IEE, Vol. 119, No 9, pp. 1301-1308.

Deleroi, W. Kovacs, K.P. 1990. Einfluss der Eisensättigung auf die

Hauptfeldverteilung in Drehfeldmaschinen am Beispiel der Inductionsmaschine. ETZ-A Bd. 12, (1990) H.11, S. 363-370.

Freeman, E.M. 1968. Travelling waves in induction machines: input impedance and equivalent circuits. Proc. IEE Vol. 115, No 12, pp. 1772-1776.

Freeman, E.M. 1974. Equivalent circuits from electromagnetic theory: low-frequency induction devices. Proc. IEE, Vol 121, No. 10, pp. 1117-1121.

Heller, B. Hamata, V. 1977. Harmonic field effects in induction machines. Amsterdam, Elsevier. 330 p.

Greig, J. Freeman, E.M. 1967. Travelling wave problem in electrical machines. Proc. IEE, Vol. 114, No. 11, pp. 1681-1683.

Jamieson, R.A. 1968. Eddy-current effects in solid, unslotted iron rotors. Proc. IEE. Vol. 115, No. 6, pp. 813-820.

Jordan, H. Raube, W. 1972. Zum Problem der Zusatzverluste in Drechstrom-Asynchronmotoren. ETZ-A Bd. 93, H10, S. 541-545.

Jordan, H. Taegen, F. 1965. Zur Messung der Zusatzverluste von Asynchronmaschinen. ETZ-A Bd. 86, H. 6, S. 167-171.

Kesavamurthy, N. Rajagopalan, P.K. 1959. The polyphase induction machine with solid iron rotor. Trans. AIEE pt. III 78, pp. 1092-1098.

Krishnamurthy, M.R. Veluchamy, V. 1972. Polyphase induction machine with hollow ferromagnetic rotor. IEEE Winter meeting N.Y. N.Y. 1972. Paper T 72 067-2, pp. 1677-1691.

Larjola, J. 1988. The principle of high speed technology. Conference on high speed technology, Lappeenranta, Finland, August 21-24, 1988. Lappeenranta. Lappeenranta Univ. of Technology, Department of Energy Technology, pp. 11-28.

Liese, M. 1979. Verfahren zur Berechnung von Wirberlströmen in Massivem Eisen. Archiv für Elektrotechnik 59, S. 75-85.

MacLean, W. 1954. Theory of strong electromagnetic waves in massive iron. Journal of applied physics 25, pp. 1267-1270.

Pillai, K.P.P. 1969. Fundamental-frequency eddy-current loss due to rotating magnetic field. Proc. IEE, Vol. 116, No. 3, pp. 407-410.

Pipes, L.A. 1956. Matrix theory of skin effect in laminations. Journal of the Franklin Institute, 262, pp. 127-138.

Rajagopalan, P.K. Balarama Murty, V. 1969. Effects of axial slits on the performance of induction machines with solid iron rotors. IEEE Trans. PAS 88, 11, pp. 1695-1709.

Richter, R. 1954. Elektrische Maschinen IV Die Induktionsmaschinen, Zweite, verbesserte Auflage, Basel/Stuttgart, Verlag Birkhäuser. 440 S.

Richter, R. 1967. Elektrische Maschinen I Allgemeine Berechnungselemente Die Gleichstrommaschinen, Dritte, erweiterte Auflage, Basel/Stuttgart, Verlag Birkhäuser. 691 S.

Riepe, F. 1981a. Eindimensionale Berechnung der Drehstrom-Asynchronmaschine mit ungenutetem Stromverdrängungsläufer. Archiv für Elektrotechnik 63 S. 253-259.

Riepe, F. 1981b. Zweidimensionaler rechnergestützter Entwurf von Drehstrom-Asynchronmaschinen mit massiven Läufern. ETZ-A, Bd. 3, H. 3, S. 71-75.

Wei, Bing-qui. 1987 Asynchronous motor with solid rotor of copper-iron alloy. Third Int. Conf. on Electrical Machines and Drives, London, UK, 16-18 November 1987. London, UK. IEE conference publication 282, pp. 150-152.

Wiart, A. 1982. New high-speed high-power machines with converter power supply. Motorcon September 1982, proceedings, pp. 354-365.

Woolley, I. Chalmers, B.J. 1973 End effects in unlaminated-rotor induction machines. Publ. IEE, Vol. 120, No. 6, June 1973. pp. 641-646.

Yamada, H. 1970. Calculation of torque characteristics of solid-rotor induc machine. Electrical engineering in Japan, Vol. 90, No. 2, pp. 1-9.

Yee, H. 1971. Effects of finite length in solid-rotor induction machines. Proc. I Vol. 118, No. 8, pp. 1025-1033.

Yee, H. Wilson, T. 1972. Saturation and finite-length effects in solid r induction machines. Proc. IEE, Vol. 119, No. 7, pp. 877-882.

Ylinen, A. 1970. Kimmo- ja lujuusoppi I-II, 2. uudistettu painos. Porvoo, WSO s. 1010.